

DR#0474-X

89/10/88 85 (2)
PPPL-2510
qc-420

PPPL-2510


REPRODUCED FROM
BEST AVAILABLE COPY

TIME-DEPENDENT SIMULATIONS OF A COMPACT IGNITIC TOKAMAK

By

D.P. Stotler and Glenn Bateman

MAY 1988

PLASMA
PHYSICS
LABORATORY 

PRINCETON UNIVERSITY
PRINCETON, NEW JERSEY

PREPARED FOR THE U.S. DEPARTMENT OF ENERGY,
UNDER CONTRACT DE-AC02-76-CMO-3073.

DISCLAIMER

This report was prepared as an account of work sponsored by an agency of the United States Government. Neither the United States Government nor any agency thereof, nor any of their employees, makes any warranty, express or implied, or assumes any legal liability or responsibility for the accuracy, completeness, or usefulness of any information, apparatus, product, or process disclosed, or represents that its use would not infringe privately owned rights. Reference herein to any specific commercial product, process, or service by trade name, trademark, manufacturer, or otherwise does not necessarily constitute or imply its endorsement, recommendation, or favoring by the United States Government or any agency thereof. The views and opinions of authors expressed herein do not necessarily state or reflect those of the United States Government or any agency thereof.

Time-Dependent Simulations of a Compact Ignition Tokamak

D. P. Stotler and Glenn Bateman
Plasma Physics Laboratory
Princeton University
Princeton, New Jersey 08543

PPPL--2510

DE88 011170

ABSTRACT

Detailed simulations of the Compact Ignition Tokamak are carried out using a 1-1/2-D transport code. The calculations include time-varying densities, fields, and plasma shape. It is shown that ignition can be achieved in this device if somewhat better than L-mode energy confinement time scaling is possible. We also conclude that the performance of such a compact, short-pulse device can depend greatly on how the plasma is evolved to its flat-top parameters. Furthermore, in cases such as the ones discussed here, where there is not a great deal of ignition margin and the electron density is held constant, ignition ends if the helium ash is not removed. In general, control of the deuterium - tritium density is equivalent to burn control.

MASTER

I. Introduction

In this paper we discuss transport simulations of the Compact Ignition Tokamak (CIT).¹ The flat-top parameters used in this work are given in Table I. The goal of CIT is to study an ignited plasma in a device of minimum cost; this necessarily restricts the size of the device. Despite being comparable (e.g., DIII-D²) or smaller (e.g., TFTR³ or JET⁴) in size than existing experiments, CIT is expected to exhibit better performance due to the considerably higher fields and densities planned. Evaluation of the design requires significant extrapolations of the experimental data base. Given these extrapolations, we can use transport simulations to make detailed predictions about the performance of CIT. The primary assumptions involve describing the particle and thermal transport. There are also limits placed on the plasma density, β (ratio of the plasma energy to the magnetic energy), and fusion power that must be adhered to in exploring the operating space of CIT. Note that these simulations not only aid in the design of the machine itself and help to identify critical issues, but also provide parameters for diagnostic design. Furthermore, other theoretical groups can utilize the plasma profile and equilibrium information to perform more involved calculations (e.g., stability).

Although we focus here on CIT, the techniques and some of the results can be applied to tokamaks in general. As examples of the utility of transport codes, we point out that they are useful in analyzing and understanding experimental results,⁵⁻⁷ and have also been employed in predicting the performance of other ignited tokamaks.^{8,9}

In this paper, we show that the way in which the plasma is grown onto the divertor during the current ramp can have an impact on the fusion power production in CIT by way of controlling the size of the sawtooth mixing radius. This effect is important for CIT since the resistive skin time is long compared to the pulse length. For a steady-state reactor, these considerations are not likely to be as significant except to point out the utility of some form of current profile shaping. We also find that even at modest power production levels, helium ash accumulation (for constant electron density) can quench the ignition. In CIT, this may just provide a convenient form of burn control. Of course, if the density cannot be regulated in the actual experiment, some other form of active burn control may be required. In a general reactor,

helium accumulation may be just as much of a problem. Such devices will require a scheme for removing helium as it is formed in order to maintain an extended burn phase.

We will next briefly describe our transport code and some of the CIT simulations that have been performed previously. In Section II, we describe in detail the models and assumptions used in the present work. Then, in Section III we will discuss the results of two specific simulations. We will address a few sensitivity issues that were not discussed in the previous work¹⁰ in Section IV. Finally, we present our conclusions in Section V.

The code we use to perform the simulations has been described in detail elsewhere.^{11,12} In particular, we employ the 1-1/2-D BALDUR transport code. It integrates over time a set of flux-surface-averaged transport equations on a radial grid of flux surfaces; the shape of the flux surfaces is provided by a moments equilibrium code interfaced with the transport code. The equations solved describe diffusion of density, energy, and magnetic field:

$$\left. \frac{\partial}{\partial t} \right|_{\xi} (nV') = -\frac{\partial}{\partial \xi} (V' \langle \Gamma_{\rho} \cdot \nabla \xi \rangle - nV' \dot{\rho} / \rho') + V' \langle S \rangle, \quad (1)$$

$$\begin{aligned} \left. \frac{3}{2} \frac{\partial}{\partial t} \right|_{\xi} (nTV') &= -\frac{\partial}{\partial \xi} \left(V' \langle q_{\rho} \cdot \nabla \xi \rangle - \frac{3}{2} \frac{nTV' \dot{\rho}}{\rho'} \right) \\ &+ V' \langle Q \rangle - nT \left[\dot{V}' - (\dot{\rho} V' / \rho') \right], \end{aligned} \quad (2)$$

$$\begin{aligned} \left. \frac{\partial}{\partial t} \right|_{\xi} (B_p \rho') &= \frac{\partial}{\partial \xi} \left\{ \frac{\eta}{I(1/R^2)} \left[\frac{I^2}{\mu_0 V'} \frac{\partial}{\partial \xi} \left(\frac{V' \rho' B_p}{I} \left\langle \frac{|\nabla \xi|^2}{R^2} \right\rangle \right) \right. \right. \\ &\quad \left. \left. - \frac{\langle \mathbf{J}_{beam} \cdot \mathbf{B} \rangle}{R_{OREF}} - \frac{\langle \mathbf{J}_{boot} \cdot \mathbf{B} \rangle}{R_{OREF}} \right] + \dot{\rho} B_p \right\}. \end{aligned} \quad (3)$$

There are separate equations for the density, $n(\xi, t)$, of each ionic species; the electron density is computed from quasi-neutrality. Separate energy equations are solved for ions and electrons; the temperatures, $T(\xi, t)$, of all ionic species are taken to be equal. The quantity appearing in Eq. (3) is actually a normalized poloidal flux gradient:

$$B_p \equiv \frac{\partial \psi_{pol} / \partial \rho}{2\pi R_{OREF}}. \quad (4)$$

In the limit of a circular cylinder geometry, this B_p reduces to the actual poloidal magnetic field. Note that ρ is a flux-surface label defined by $\rho \equiv (\psi_{tor}/\pi B_{0REF})^{1/2}$; B_{0REF} and R_{0REF} are a fixed reference magnetic field and major radius. The equations have been transformed into a coordinate system with arbitrary flux surface label ξ ; the toroidal (poloidal) fluxes are denoted by ψ_{tor} (ψ_{pol}). The volume inside flux surface ξ is $V(\xi, t)$; $V' = \partial V/\partial \xi$. An overdot indicates a derivative with respect to time. The particle and heat fluxes are designated as Γ_ρ and q_ρ ; the subscript ρ signifies that they are defined relative to surfaces of constant toroidal flux. Volume sources of particles (energy) are contained in S (Q). Finally, in the magnetic diffusion equation, Eq. (3), R is the major radius, η is the plasma resistivity, and $I(\xi) = RB_T$, where B_T is the toroidal magnetic field. The code is able to treat beam-driven current (J_{beam}) and bootstrap current (J_{boot}). In all cases, the angle brackets denote a flux-surface average.

The full expressions for the fluxes and sources are quite complicated¹¹ and will not be given here. Instead we will specify below the semi-empirical (anomalous) transport coefficients used to predict the level of particle and energy confinement in CIT. The present version of BALDUR is capable of treating sawtooth oscillations, ballooning modes, and bootstrap current.

The work discussed here is an extension of previous investigations; Singer et al.¹⁰ carried out the original simulations upon which these are based. One of their primary conclusions was that uncertainties in the experimentally calibrated transport model lead to significant variations in the predicted performance of CIT; this is still true in the present study. Since then, there have been numerous changes to the CIT design, the BALDUR code, and to the details of the plasma programming used in the simulations. Instead of relying on a semi-empirical transport model completely as done before, we alter the overall magnitude of the local transport coefficients to yield global confinement times between those expected for the L-mode and H-mode¹³ (i.e., a confinement time twice that of L-mode; see, for example, Ref. 14) as computed using the scaling of Kaye and Goldston.¹⁵ The detailed profile and transient behavior information contained in the original transport models is retained in this manner and does have a significant impact on the simulations. The transport models we use here were calibrated against L-mode discharges; hence, we cannot use them to accurately predict performance during H-mode operation. Instead, we view this procedure as one of enhancing an L-mode

discharge. The previous conclusions regarding uncertainties in the transport model remain.

II. Models and Assumptions

We now describe the time dependence of the discharge parameters that are input to the code, as well as the transport models, the auxiliary heating scheme, and the MHD effects treated here. The bootstrap current is a recent addition to the 1-1/2-D BALDUR code; its effects will also be discussed in this paper.

A. Parameters

In Fig. 1 we show how the toroidal magnetic field, B_T ; plasma current, I_p ; elongation κ and triangularity δ of the 95% toroidal flux surface; and volume-averaged electron density, $\langle n_e \rangle$, evolve as a function of time. The simulation starts with an almost circular shape and non-zero fields. By $t = 3$ sec, the plasma is on the divertor (at full elongation), and at $t = 5.8$ sec, all fields have reached their flat-top values (shown also in Table I). Note that the auxiliary heating extends from $t = 4.8$ to $t = 6.3$ sec. The time evolution of the plasma shape is more clearly indicated in Fig. 2; these equilibrium flux contours are from the fast ramp case described in Sec. III.B. The design flat-top is limited to five seconds in duration by resistive heating of the toroidal field coils. Very few of our simulations are still ignited at this point. So for present purposes, a longer flat-top is unnecessary. For simplicity, we do not consider the shut-down phase of the discharge here. Studies of this period in CIT are very critical, however, in order to avoid disruptions resulting from exceeding the density limit or MHD stability limits.

The magnetic field is ramped up such that the toroidal magnetic energy is increasing approximately linearly with time (toroidal magnetic field goes like the square root of time). On the other hand, the plasma current and shape parameters rise in a purely linear fashion. This particular ramp scheme is based upon work done by Pomphrey and Jardin.¹⁶ Their primary concern is with the design of the field coils used to determine and control the plasma shape. As will be discussed in Section III.B, the details of this ramp scheme can affect the plasma evolution and stability during flat-top. The results of

our simulations can provide feedback that is useful in designing the actual plasma ramp scheme.

Like the current, the electron density is brought up (approximately) linearly. This strategy is based upon the empirical observation that the maximum allowable electron density is proportional to the plasma current. In particular, the Murakami - Hugill density limit^{17,18} is usually written as $\langle n_e \rangle_{MH} \propto B_T / (Rq_{cyl})$ (i.e., proportional to the total plasma current). When $\langle n_e \rangle_{MH}$ is expressed in 10^{20} m^{-3} , B_T is in T, and R is in m, the constant of proportionality is of order unity. However, due to the scarcity of experimental data in elongated geometries, there is some uncertainty as to exactly what expression should be used for q_{cyl} . The safety factor of an equivalent circular cylinder is $q_{cyl} = 5a^2 B_T / (RI_p)$, with a , the minor radius, and R in m, B_T in T, and I_p in MA. In extending the definition of q_{cyl} to elongated geometries, one generally multiplies this expression by some function of κ and δ that is of order unity and reduces to unity in the circular limit. A popularly used expression multiplies q_{cyl} by $[1 + \kappa^2(1 + 2\delta^2)]/2$; in this case, a constant of proportionality of 1.5 leads to $\langle n_e \rangle_{MH} = 2.8 \times 10^{20} \text{ m}^{-3}$. On the other hand, if just the original circular expression for q_{cyl} is employed, the limit increases to $8.9 \times 10^{20} \text{ m}^{-3}$. There is some evidence¹⁹ that the higher limit may in fact be the more appropriate one. However, in the absence of an adequate model for the density limit, we have tried to remain close to the smaller value.

The sharp changes in the electron density are the result of large pellets composed of equal amounts of deuterium and tritium being shot in with velocities of 2 km/sec (except for the first one done at 1.5 km/sec). The timing is such that the last one goes in during the auxiliary heating; it does not penetrate to the inner regions of the plasma. In general, pellet penetration is a problem for smaller or slower pellets once the plasma becomes energetic and dense. In between the pellets, the electron density is maintained at the constant level indicated in Fig. 1 by balanced deuterium and tritium gas puffing at the edge.

We also include two impurity species in these simulations. The first is helium; it accounts not only for the thermalized alpha particles, but also the He^3 required for the planned auxiliary heating scheme (see Sec. II.D). For the latter purpose, we influx sufficient helium between $t = 3.1$ and $t = 4.7$ sec to reach the approximate concentration of 5% desired for efficient heating. The primary impurity is assumed to be carbon, consistent with the use of

graphite tiles to cover the interior of the vacuum vessel. Initially, there is enough carbon present to yield $Z_{eff} = 1.5$. We define

$$Z_{eff} \equiv \frac{\sum_j n_j \langle Z_j^2 \rangle}{n_e}, \quad (5)$$

where the sum is over all ionic species; their densities and charges are designated as n_j and Z_j , respectively. The angle brackets denote an average over the coronal equilibrium charge states. During pellet injection, Z_{eff} drops steadily up to the initiation of auxiliary heating. From this point until $t = 8.3$, we influx carbon, bringing Z_{eff} back to about 1.5. Typically, Z_{eff} continues to increase due to helium ash accumulation, adding as much as another 0.1 to Z_{eff} . The boundary conditions for all impurities constrain the particle flux at the plasma edge. The code is set up so that except during periods of user-specified influx (or outflux), the number of impurity particles is constant.

B. Transport Models

We now give expressions for the particle and energy fluxes appearing in Eqs. (1) and (2). In this particular version of BALDUR the flux-surface label, ξ , is taken to be the square root of the normalized toroidal flux, $\xi = \sqrt{\psi_{tor}/\psi_{tor,a}}$, where $\psi_{tor,a}$ is the toroidal flux at the plasma boundary.

The particle flux of ionic species j is written as

$$\langle \Gamma_p \cdot \nabla \xi \rangle_j = \left(-D_j \frac{\partial n_j}{\partial \xi} \langle |\nabla \xi| \rangle + n_j v_j + \Gamma_j^{neo} \right) \frac{\langle |\nabla \xi|^2 \rangle}{\langle |\nabla \xi| \rangle}, \quad (6)$$

and we assume

$$D = \frac{1}{n_e(\xi)/(10^{19} \text{ m}^{-3})} \text{ m}^2/\text{sec},$$

$$v = -2Dr/a^2;$$

r is a generalization of the minor radial coordinate. Here, r is defined as half of the width (the half-width) of a given flux surface on the midplane; it is thus a flux surface quantity. The neoclassical flux, Γ_j^{neo} , includes the Ware pinch for the hydrogenic components. The detailed expressions are given in Ref. 11. The inward pinch used here²⁰ simulates the density peaking

effect one hopes to achieve with pellet injection.²¹ As will be demonstrated below, the density profiles we get with this transport model are centrally peaked, particularly for cases with narrow sawtooth oscillations. Since this is beneficial to ignition,²² it might be argued that we are being overly optimistic. However, by making this (not unusual) assumption, we are able to ignite with relatively conservative specifications on auxiliary heating and confinement time (see Sec. III.A).

The expression we use for the heat flux is

$$\langle q_\rho \cdot \nabla \xi \rangle_j = \left(-\chi_j \frac{\partial}{\partial \xi} \left\langle \frac{3}{2} n_j T_j \right\rangle \langle |\nabla \xi| \rangle + \frac{3}{2} T_j \langle \Gamma_\rho \cdot \nabla \xi \rangle_j \right) \frac{\langle |\nabla \xi|^2 \rangle}{\langle |\nabla \xi| \rangle}, \quad (7)$$

where the subscript j denotes electron or ion thermal flux. We will make use of the following two semi-empirically derived thermal diffusivities, χ_j .

The first one was developed by Singer, Ku et al.,²³ and used in the original simulations of CIT with BALDUR.¹⁰ They actually obtained a family of scaling laws; the one we employ here is proportional to temperature. In particular,

$$\chi_e^{SK} \propto \frac{r}{R^2 \kappa^4 n_e^{0.875}} \left[\frac{P_{th}/n_e^{0.95}}{(B_r r^{0.5}/q)^{0.8} Z_{eff}^{0.4}} \right] \left| \frac{\partial \ln P_{th}}{\partial \ln r} \right|^{1/2}, \quad (8)$$

$$\chi_i^{SK} = 0.5 \chi_e^{SK} + \chi_i^{CH}, \quad (9)$$

where P_{th} is the thermal pressure, and q is the local MHD safety factor. The neoclassical contribution computed by Chang and Hinton²⁴ is included as χ_i^{CH} . Note that the expression in square brackets is approximately constant for ohmic plasmas. Singer et al.²³ determined the constant of proportionality in Eq. (8) to be $2.1 \times 10^{33} \pm 33\%$ (all quantities in SI units) by comparison with experimental data.

We will compare results for the global energy confinement time, τ_E , obtained using one of our two semi-empirical models with a reference confinement time, $\tau_{E,KG}$. Specifically, $\tau_{E,KG}$ is an inverse quadratic combination²⁵ of a neo-Alcator ohmic scaling and the Kaye-Goldston¹⁵ auxiliary heated scaling:

$$\frac{1}{\tau_{E,KG}^2} = \frac{1}{\tau_{NA}^2} + \frac{1}{\tau_{AUX}^2}, \quad (10)$$

where

$$\begin{aligned}\tau_{NA} &= 7 \times 10^{-3} \bar{n}_{e,19} a R^2 q_{cyl}, \\ \tau_{AUX} &= \tau_{AUX,KG} \times \left(\frac{A_1 A_2}{A_D A_H} \right)^{0.25}, \\ \tau_{AUX,KG} &= 3.04 \times 10^{-2} \kappa^{0.28} B_T^{-0.09} I_p^{1.24} P_{tot}^{-0.58} (\bar{n}_{e,19})^{0.28} a^{-0.49} R^{1.65},\end{aligned}$$

and

$$q_{cyl} = 5 \frac{i^2 B_T}{I_p R} \left[\frac{1 + \kappa^2 (1 + 2\delta^2)}{2} \right]. \quad (11)$$

Here, $\bar{n}_{e,19}$ is the line-averaged electron density in units of $10^{19} m^{-3}$. The minor and major radii in m are denoted by a and R . The magnetic field, B_T , is in T, and I_p is the plasma current in MA. The total power, P_{tot} , (alpha, ohmic, and auxiliary) is in MW. The additional mass factor added to τ_{AUX} represents one possible scaling for the mass dependence of the energy confinement time.^{26,27} In this expression, A_i is the mass of species i ; 1 and 2 refer to the main components of the plasma under consideration; D and H are for deuterium and hydrogen, respectively.

We have adjusted the coefficients of the thermal transport models employed in the simulations so that they yield confinement times between $\tau_{E,KG}$ (L-mode) and $2\tau_{E,KG}$ (H-mode). For the Singer-Ku model, this amounted to using a coefficient 1.25 times larger than their original calibration (2.1×10^{23}); this is within their error bars.²³

Our second transport scaling was developed by Redi, Tang, et al.⁵ Since the detailed expressions for the thermal diffusivities are quite complicated, we refer the reader to the original work for more information. This model assumes profile-consistency. In particular, the electron temperature profile is taken to have a Gaussian shape determined only by the edge safety factor. This constraint is used to derive a radial form factor for the thermal diffusivity. By comparing this expression with the predictions of the turbulent transport due to microinstabilities in an appropriate region of the plasma, the overall magnitude can be fixed. The modes focussed on are the trapped electron drift wave for χ_e and the toroidal ion temperature gradient driven instability for χ_i . Depending upon the collisionality, χ_e can have one of two forms; for the highly collisionless case ($\nu_{ee} < 0.15$, with ν_{ee} evaluated at the $q = 1.5$ surface),

$$\chi_e^{collisionless} \propto P_{e,tot}^{0.6}(a);$$

while for more collisional plasmas ($\nu_{*e} > 0.15$),

$$\chi_e^{c'at} \propto P_{e,tot}^{0.8}(a).$$

Here, $\nu_{*e} = \nu_{eff}/\omega_b$, with ν_{eff} and ω_b denoting the effective collision and trapped electron bounce frequencies, respectively. In the above expressions, $P_{e,tot}(a)$ is the total power input into the electrons integrated over the plasma. Unlike the original model, the transition between the two scalings is smoothed somewhat.

The contribution from the ion temperature gradient driven modes, $\chi_i^{\eta_i}$, is added on to the neoclassical expression of Chang and Hinton²⁴ to form the χ_i that goes into Eq. (7). When $\eta_i \equiv \partial \ln T_i / \partial \ln n_i > 1.5$ (also evaluated at the $q = 1.5$ surface),

$$\chi_i^{\eta_i} \propto P_{i,tot}^{0.8}(a),$$

where $P_{i,tot}$ is the total power input to the ions; otherwise, $\chi_i^{\eta_i} = 0$. Again, this transition is smoothed somewhat in the present work, contrary to the procedure used in the original calibration.

The overall coefficients for these three scaling laws, $\chi_e^{c'less}$, $\chi_e^{c'at}$, and $\chi_i^{\eta_i}$ have been adjusted in the simulations by a constant factor to yield global confinement times between $\tau_{E,KG}$ and $2\tau_{E,KG}$ to reflect the enhanced confinement observed in diverted tokamaks.

The fundamental distinctions between the Redi-Tang model and the Singer-Ku model lead to noticeable differences in the results despite the somewhat similar confinement times. Most notably, the Singer-Ku model scales with the plasma energy while the Redi-Tang expression increases with the power input into the plasma. When thermal transients are present (e.g., the sudden initiation of auxiliary heating), the Redi-Tang model will instantly show a degradation in confinement time. On the other hand, a transport model scaling with energy content such as χ_e^{SK} may take a while to exhibit a drop in confinement, and can in fact actually give rise to a temporary increase in τ_E . The other way in which the two approaches differ is in the resulting temperature profile shape. We will say more about this distinction in Sec. III.B.

C. MHD and Neoclassical Effects

Sawtooth oscillations in BALDUR are modelled using a Kadomtsev reconnection picture.^{22,28} Of course for there to be a reconnection, the safety factor on axis must be less than unity. When it is, the code periodically flattens the density and temperature profiles out to the mixing radius; there is no (direct) alteration of the exterior portion of the plasma. The value of the mixing radius is computed from the Kadomtsev theory²⁸; it is typically 20 to 40% larger than the radius of the $q = 1$ surface. Since detailed models for the periodic trigger mechanism of the sawtooth oscillations are not available, the user is required to specify the period on input. For all of the simulations discussed here, it is fixed at 0.3 sec.¹⁰ The importance of sawtooth oscillations in CIT will be discussed in Sec. III.B.

BALDUR can also be instructed to compute the critical pressure gradient for ideal MHD ballooning modes using information from the equilibrium code. Furthermore, there is a mechanism for enhancing the thermal diffusivity on unstable flux surfaces, as was suggested by Connor, Taylor, and Turner²⁹ and Azumi et al.³⁰ We refer the reader to Ref. 9 for details on the solution of the ballooning mode equation, the implementation of the enhanced transport, and the effects of low shear. The purpose of this procedure is solely to constrain the profiles to remain stable with respect to these modes; the effects on CIT will be described in Sec. IV.A.

BALDUR has been recently upgraded to include the neoclassical bootstrap current effect. Its implementation is described in more detail in Ref. 9. The expressions used can be shown to be similar to those found in Refs. 31 and 32. We will discuss its relevance to CIT in Sec. IV.C.

D. Auxiliary Heating

In order to reach ignition, the CIT design¹ calls for 10 - 20 MW of ion cyclotron resonance heating (ICRH). Present plans are to use He^3 minority and tritium second harmonic heating. Since self-consistent computations of the deposition profile for ICRH are beyond the scope of the BALDUR code, we must provide heating information based upon studies done elsewhere. In order to maintain a realistic accounting of impurity species, we influx the 5% of He^3 ($n_{He}/n_e = 0.05$) needed for efficient minority heating.

For all of the simulations discussed here, auxiliary heating begins at $t = 4.8$ sec and ends at $t = 6.3$ sec. Although the toroidal field is changing during the first 1 sec of this period, the resonance layer does not move appreciably (< 0.05 m). We hold the location of the peak of the heating profile fixed throughout for simplicity (although the code is capable of modelling a moving profile³³). The operating frequency of the antenna is assumed to be adjusted so that the peak of the heating is at the magnetic axis; this should be the optimum configuration for energy confinement.

At the densities planned for CIT, the focussing effect of the plasma on the incident ICRH waves is expected to be significant.³⁴ The theoretically predicted shape of the profile is uncertain apart from this information. Here, we use a fixed, Gaussian-shaped deposition profile that drops to half of its central value at $r \simeq 0.15$ m.

The other information required to specify the auxiliary heating is the relative amount of power going into the electron and ion channels. Fortunately, this can be computed with a bit more confidence; in particular, we expect³⁵ $P_i/P_e \sim 2/1 - 3/1$, where P_i and P_e refer to the power into the ions and electrons, respectively. We follow the work by Singer et al.¹⁰ and assume that the ions receive 75% of the input power.

Although 20 MW should be available for CIT operation, we will restrict ourselves to a more conservative 10 MW for all of the simulations presented here. Furthermore, we use throughout a 1.5 sec heating time. In previous work, longer heating periods and higher power levels were employed.^{10,33} This limits the range of temperatures and densities that we can examine due to the finite amount of time required to heat to ignition temperatures given the expected losses. Nonetheless, we still predict that CIT will ignite.

III. Results

We now discuss in detail the results of two simulations performed using the models described above. The primary distinction between the two is the expression for the thermal diffusivity. The first (referred to hereafter as I) uses the Singer-Ku model, while the second (II) follows the Redi-Tang approach. The evolution of the volume-averaged electron density for I is as shown in Fig. 1 with a flat-top value of $\langle n_e \rangle = 3.0 \times 10^{20} \text{ m}^{-3}$. For simulation II, we retain the basic form of the time evolution, but rescale everything to

reach a maximum density of $\langle n_e \rangle = 3.4 \times 10^{20} \text{ m}^{-3}$. The higher density is needed to reach ignition with this more pessimistic transport model. Finally, we enhance the thermal transport on ballooning-unstable flux surfaces in simulation I, but not in II. We will discuss this procedure and its effect on ignition in Sec. IV.A.

A. Ignition Parameters

In Figs. 3 and 4, we show the time evolution of the different contributions to the input power for each of the two simulations. The ohmic power rises during the current ramp; the small spikes are the result of the temperature drops accompanying each pellet injection. Once the auxiliary heating is turned on and the electron temperature rises above a few keV, the ohmic power falls; it levels off at a flat-top value of 1 - 2 MW.

As mentioned previously, both runs assume that 10 MW of auxiliary power is being absorbed between $t = 4.8$ sec and $t = 6.3$ sec. During this period, and particularly following the injection of the last pellet at $t = 5.6$, the fusion power rises sharply. Ignition is indicated in both simulations by the continued increase of the alpha power, P_α , following the termination of auxiliary heating. The end of ignition (negative net power into the plasma) occurs at about the time P_α peaks. We will discuss the reasons why the discharges did not run away in Sec. III.C. Wall loading considerations require us to limit CIT to a time-averaged alpha power during the burn phase of $P_\alpha \simeq 60$ MW; both of these runs are clearly below this value. The jagged shape of the alpha power curve for simulation II is the result of the sawtooth oscillations. This effect does not appear in I due to the ballooning-enhanced transport which forces the temperature profile to remain relatively flat in the center part of the plasma even between sawteeth in order to stay close to marginal stability with respect to high- n ballooning modes.

The ballooning instability in simulation I is localized inside the sawtooth mixing region ($\sim 25\%$ of the minor radius). It is likely that this low-shear, $q \simeq 1$ area is also unstable in II. Note, however, that the volume-averaged toroidal β values are well below the Troyon limit^{36,37} of $\beta_T \equiv 3I_p/aB_T\%$ (where I_p is in MA, a in m, and B_T in T). The reason for this is that the pressure profiles are not optimized with respect to ballooning modes as are those upon which the Troyon limit is based. For CIT parameters, $\beta_T = 4.9\%$.

In simulation I, we find a peak total $\beta = 3.8\%$ and in II, $\beta = 2.7\%$. These correspond to $\beta/\beta_T = 0.77$ and 0.55 , respectively.

We show in Fig. 5 the β due to fast alpha particles in simulation I as a function of time and plasma half-width. This profile is much more peaked than the thermal pressure profile due to the fact that $P_\alpha \sim n_D n_T T_i^2$. For this run, the volume-averaged contribution from fast alphas peaks at $\beta_\alpha = 0.45\%$; in II, we find $\beta_\alpha = 0.21\%$.

The evolution of the global energy confinement time, τ_E , for the two simulations is illustrated in Fig. 6. In both cases, pellet injection gives rise to significant changes in confinement. The Singer-Ku transport model typically comes very close to matching neo-Alcator scaling during the ohmic portion of the discharge. This is evidenced in part by the sharp rises in τ_E at the times of pellet injection ($\tau_{NA} \propto \bar{n}_e$). During auxiliary heating, the pellets cause a drop in T that locally decreases thermal transport. With regard to the Redi-Tang model in simulation II, the pellets alter considerably the temperature and density profiles and, hence, lead to changes in the ν_{*e} and η_i values that are used to choose the thermal diffusivity scaling. Note that in this case the improvement in confinement following pellet injection one expects from the ion channel is not clearly evident. Due to the lack of deep penetration here, the density profile does not peak up sufficiently to raise η_i above the critical value of 1.5 needed to turn off the η_i mode transport.

The confinement time in simulation II during the ohmic phase is above the neo-Alcator value. However, the plasma conditions just prior to the initiation of auxiliary heating are not much different from those of simulation I, and the plasma energy at this point is small relative to that added by auxiliary and alpha heating. So, we are confident that we are not being overly optimistic in using this transport model during the early stages of the run.

Upon initiation of auxiliary heating, there are again sharp changes in confinement in both cases. Furthermore, the responses are in opposite directions. In the Tang-Redi transport model, all thermal diffusivities scale with input power and thus show an instantaneous degradation in confinement when the heating is turned on. On the other hand, because χ_e is proportional to the local temperature in the Singer - Ku model used in simulation I and the heating deposition profile is centrally peaked, we initially see the plasma energy rising rapidly in the center, but remaining relatively fixed near the edge. It is the edge losses that enter into the global $\tau_E = W_{tot}/P_{loss}$. Since they do

not respond to the central heating immediately while the volume-integrated energy, W_{tot} , does, the confinement time actually rises at first. This is true until the centrally deposited energy diffuses out to the edge. Because of the pellet injection at $t = 5.6$ sec, this effect is somewhat obscured in Fig. 6; note, however, that τ_E is dropping just prior to termination of the auxiliary heating.

In both cases, the degradation (improvement) of confinement with increasing (decreasing) alpha power is clear during the burn phase. The oscillations in the curve for simulation II are due to the effects of the broad sawteeth. Because of the ballooning-enhanced transport, these oscillations do not appear in simulation I.

To get an idea of how the confinement times compare with presently acknowledged scaling laws, let us make a few computations using flat-top parameters. In both cases, $\tau_{NA} \simeq 1.1$ sec. With $P_{tot} = 60$ MW (simulation I), we have from Eq. (10), $\tau_{E,KG} \simeq 0.45$ sec. At this point in the run, $\tau_E \simeq 0.65$ sec, so $\tau_E/\tau_{E,KG} \simeq 1.4$. In this simulation, the ratio $\tau_E/\tau_{E,KG}$ is as high as 2.0 during heating; drops steadily during the burn phase, reaching 1.4 near the end of the discharge. The power level is lower in II, $P_{tot} \simeq 45$ MW. We calculate $\tau_{E,KG} \simeq 0.52$ sec and $\tau_E/\tau_{E,KG} \simeq 1.4$ with $\tau_E \simeq 0.7$ sec. For this case, the ratio $\tau_E/\tau_{E,KG}$ is close to 1.3 - 1.4 throughout the heating and burn phases of the discharge.

Despite the significantly different transport models, and the contrasting profiles that result, these two simulations are qualitatively similar in many respects (for example, see Figs. 3 and 4). This similarity is in part the result of having about the same density and confinement time for both runs.

B. Effects of Sawtooth Oscillations

As has been noted previously,^{9,22} peaked profiles increase the size of the window in density - temperature space for ignited operation. This is primarily due to the fact that $P_\alpha \propto n_D n_T T_i^2$. That is, with peaked profiles, the central density and temperature are higher for a given volume-averaged energy than with flat profiles and, hence, so is the volume integral of $n_D n_T T_i^2$ (i.e., the total alpha power). The time-averaged effect of sawtooth oscillations is to flatten the density and temperature profiles. Hence, they can have a deleterious effect on ignition if they are too broad.

Bateman²² discussed a way to delay significantly the appearance of sawtooth oscillations using a combination of pellet injection and current ramp. Here, we extend this concept and consider factors that might have an impact on the breadth of the sawteeth. In particular, we examine the effects of the thermal transport model and the start-up scenario.

In Figs. 7 - 10, we show the ion temperatures and electron densities from our two simulations. The spikes in the electron density during the first six seconds of the discharge are the result of pellet injection. The relatively peaked profile in Fig. 7 is due to the inward particle pinch and the maintenance of relatively narrow sawtooth oscillations; in this case the sawtooth mixing radius is $r_{mix}/a \simeq 0.25$. In contrast, the profile shown in Fig. 8 is flat during the burn phase even with the same particle pinch; here, $r_{mix}/a \simeq 0.60$. These sawteeth are large enough to have an impact on the energy confinement time (see Fig. 6). Despite the higher volume-averaged electron density ($3.4 \times 10^{20} m^{-3}$ versus $3.0 \times 10^{20} m^{-3}$), the central density in simulation II is actually smaller. The central density is an important quantity in computing the total alpha power as is demonstrated by the lower fusion output in the second run.

The sawtooth oscillations also affect the ion temperature. Note, however, that there are little or no oscillations visible in Fig. 9. This is due not only to the narrow sawteeth, but also to the ballooning-enhanced transport occurring inside the sawtooth mixing region (see Sec. IV.A). The ballooning-enhanced transport is not active in case II; this allows the broad sawteeth to combine with rapid heating by the alpha particles to produce large amplitude oscillations appearing during the burn phase; see Fig. 10.

Before proceeding any further, we would like to point out that the results of this section are dependent on our choice of sawtooth model (see Sec. II.C). For example, our conclusions would not apply if the actual sawteeth do not flatten the profiles completely inside some surface near $q = 1$, but instead produce only a localized flattening. In addition, the length of the sawtooth period can also be questioned since there are no reliable predictions for it. In the case of narrow sawteeth, the magnitude of the period is unimportant.¹⁰ For broad sawteeth, moderate variations in period should not lead to large changes in the results.⁹

The breadth of the sawtooth oscillations is determined by the shape of the safety factor profile which is related to the current density [or the poloidal

field variable, B_p , evolved according to Eq. (3)]. Even below ignition temperatures (e.g., a few keV), the resistive skin time for CIT exceeds the length of the discharge. So, the way in which the current is loaded on can affect the plasma behavior during the burn. To demonstrate this, we contrast three different start-up scenarios.

The three schemes differ only in the way we evolve the plasma shape during the ramp phase. First, we will consider a run identical to simulation I but without the bootstrap current (for clarity); this will be referred to as the fast ramp case. Secondly, we examine a discharge in which the plasma does not reach full elongation until $t = 5.8$ (slow ramp case); as before, the evolution of κ and δ is linear in time. Finally, we carry out a simulation at fixed shape; that is, the plasma starts with an elongation $\kappa = 2$.

The reason for ramping the magnetic field (in addition to minimizing resistive heating of the toroidal field coils) and plasma shape is to aid current penetration. Poor current penetration can lead to skin currents and, consequently, to disruptions.¹ These techniques have an effect even in the absence of resistivity. A brief explanation follows. We have in general $\psi_{tor,a} \simeq B_T \pi a^2 \kappa$, so that raising B_T and κ leads to an increasing toroidal flux $\psi_{tor,a}$ within the plasma. As the toroidal field is raised, each surface of constant ψ_{tor} shrinks in half-width in time. Next, note that

$$\left. \frac{\partial \psi_{pol}}{\partial t} \right|_{\psi_{tor}} = \frac{2\pi}{I(1/R^2)} \eta ((\mathbf{J} \cdot \mathbf{B}) - \langle \mathbf{J}_{beam} \cdot \mathbf{B} \rangle - \langle \mathbf{J}_{boot} \cdot \mathbf{B} \rangle). \quad (12)$$

Taking the derivative of this equation with respect to ξ yields Eq. (3). From Eq. (12), we see that if there is no resistivity ($\eta = 0$), ψ_{pol} is constant in time on a surface of constant toroidal flux. We also know that at any point in time the toroidal current contained within a flux surface, $I_p(\psi_{tor})$, is a flux surface quantity. We can simplify the rest of the argument by referring to circular geometry. In this case, $\psi_{pol} \propto aRB_p$; by Ampere's law $I_p \propto aB_p \propto \psi_{pol}/R$. Thus, if R does not change, as is the case here, then I_p is (approximately in general) constant in time for a given value of ψ_{tor} . In this way we get current penetration due to the shrinking of the constant ψ_{tor} surfaces alone.

The effects of the magnetic field and shape ramps are additive in this process. So, we expect the fixed shape scheme to yield less current penetration than the schemes with shape ramp. We could apply similar arguments to determine *a priori* the best shape ramp procedure, but the actual outcome

also depends greatly on other factors. For instance, early in the run the current profile is not completely frozen-in. To see this, consider the current density profiles shown in Fig. 11. Before $t \simeq 4$ sec, the current density peaks up noticeably between sawteeth, as shown in Fig. 11(a). At later times, the profile remains flat throughout the sawtooth period [Fig. 11(b)]. The current density profile is one of the clearest indicators of the breadth of the sawtooth mixing region.

To further elaborate on the differences between the three ramp schemes, consider the time evolution of q_{cyl} (as defined in Eq. (11)) in Fig. 12. We plot in Fig. 13 the corresponding sawtooth mixing radii as a function of time. Of course, the smaller the sawtooth mixing radius is, the more fusion power we expect due to the profile peaking effect. For $t < 4$ sec, there is a correlation between r_{mix} and $1/q_{cyl}$ in each case. Note that the mixing radius for the fast ramp scheme actually goes through a minimum at about the time q_{cyl} peaks. In the fixed shape case, the sawteeth disappear between $t \simeq 1.5$ and $t \simeq 8$ sec. During this period, the safety factor on axis, q_0 , exceeds unity. Later in the run, q_0 once again falls below unity, and the sawteeth reappear. These correlations are reminiscent of the observation²⁵ that $r(q=1)/a$ scales like $1/q_{edge}$, where $r(q=1)$ is the radius of the $q=1$ surface and q_{edge} is the edge safety factor.

As the electron temperature, T_e , begins to rise, $\eta \propto T_e^{-3/2}$ falls, and the magnetic diffusion slows. This leads to a temporary drop in the rate of change of r_{mix} for the slow and fast ramp cases.

If we take the derivative of Eq. (12) and use the definition of B_p , we obtain

$$\left. \frac{\partial}{\partial t} \right|_{\xi} (\rho' B_p) = \frac{\partial}{\partial \xi} \left[\frac{\eta}{I \langle 1/R^2 \rangle R_{0REF}} \times (\langle \mathbf{J} \cdot \mathbf{B} \rangle - \langle \mathbf{J}_{beam} \cdot \mathbf{B} \rangle - \langle \mathbf{J}_{boot} \cdot \mathbf{B} \rangle) \right]. \quad (13)$$

In other words, a higher current density gradient indicates more rapid magnetic diffusion. We see from Fig. 11(b) that the runs with the broader sawtooth oscillations have larger gradients at the edge of the mixing region. Furthermore, these large gradients exist in a region of lower T_e (larger η) than for, say, the fast shape ramp case. So, while there may be little magnetic diffusion going on with narrow sawteeth (that is, r_{mix} is not changing much), it is significant with broad oscillations. This is the trend in Fig. 13. Note

that the slow ramp case appears to be close to resistive equilibrium at the end of the run.

As expected, there is a correlation between the performance in each of the three cases and the breadth of the sawtooth oscillations. The fast shape ramp scenario evolves similarly to simulation I with a maximum $P_\alpha = 59$ MW. The fixed shape run fares slightly better: the peak $P_\alpha = 63$ MW. Furthermore, the burn lasts about a half second longer. Not surprisingly, the slow ramp case is the worst with P_α getting no higher than 22 MW; there is only a brief period following auxiliary heating during which the plasma is ignited.

Although the fixed shape case may be the most desirable as far as fusion power output is concerned, it is not from a stability standpoint. The current profile in Fig. 11(b) is clearly non-monotonic, indicative of skin currents. A check of the internal inductance values, ℓ_i , from this run indicates that it is likely to be unstable with respect to the internal kink mode.³⁹ The fast ramp case might also be susceptible to such instabilities, but a more precise stability calculation will be required to make this determination.

In general, it appears that the optimum ramp scheme would be such that q_{cyl} drops monotonically from the initial value of the shape-ramped cases to the final, flat-top state. This should provide enough current penetration to avoid skin currents, yet not drop so low in q as to yield broad sawtooth oscillations or to cause disruptions.

The ramp scheme may not be important if the electron temperature profiles resemble the ones obtained in simulation II. In simulation I, the Singer-Ku thermal transport model yields an electron thermal diffusivity, χ_e , that rises slowly from ~ 0.2 m^2/sec near the center to ~ 0.4 m^2/sec at the edge. In contrast, the Redi-Tang model leads to considerably larger edge values, $\chi_e > 1 - 2$ m^2/sec , while the central diffusivity is also on the order of 0.2 m^2/sec , or smaller. Most of the increase with radius takes place in the outer 20% of the plasma. The effects of this can be seen directly on the edge ion temperature profiles in Fig. 10 (χ_i exhibits the same characteristics so that T_e and T_i have similar shapes); this is essentially the Gaussian profile shape assumed in the Redi-Tang model. On the other hand, in the Singer-Ku transport model, T_i drops almost linearly with increasing radius.

During the flat-top phase of the discharge, $V_{loop} = \partial\psi_{pol}/\partial t$ is approximately constant in space near the edge. Hence, we have $J_{tor} \propto \eta^{-1} \propto T_e^{3/2}$, neglecting neoclassical resistivity effects. Indeed, the current density profiles

in Fig. 11 look similar to the ion temperature profile, even at $t = 3$ sec. Because of the large volume elements at the edge relative to the center, there is little current in the outer 25 - 30% of the plasma in simulation II compared to I. Since both cases utilize the same total current, case II must have more current near the magnetic axis. Again, this is apparent in Fig. 11. As a result, we compute a broader safety factor profile and greater sawtooth mixing radius in this run. The low value of J_{tor} near the edge accompanying the Redi-Tang transport model also implies a gradient that is even larger than the one noted in the slow ramp case. Hence, the magnetic diffusion is rapid, and the rate of increase of r_{mix} with time is high. Early in the current ramp, this effect is not so important, and r_{mix} evolves as in the fast ramp case (both utilize the same start-up scheme). Resistive equilibrium is reached at $t \simeq 8$ sec.

We have used the Redi-Tang model previously in simulating CIT. One of the studies attempted to mock up H-mode behavior by artificially decreasing the electron and ion thermal diffusivities near the edge.³³ In these runs, not only did we find that the energy confinement improved significantly, but also that the sawtooth mixing radii were much smaller than expected. The narrower sawteeth were a result of the broader current profiles accompanying the high edge temperatures predicted by this transport model. It is reasonable to conclude that this behavior substantiates the above arguments.

C. Effects Leading to Ignition Termination

From Fig. 3 it is clear that the ignition in simulation I ends at $t \simeq 9$ sec. This is a result of the drop in the density of deuterium and tritium ions during the burn phase (recall that the electron density is being held constant). These losses result from a combination of helium ash accumulation and displacement by influxed carbon atoms. Since the code does not allow either of these impurity species to diffuse out, both effects lead to a hydrogenic ion density that is monotonically decreasing in time. In particular, the total drop in the volume-averaged hydrogenic ion density between $t = 6.5$ and $t = 10.8$ is $\Delta(n_D + n_T) = -5.4 \times 10^{19} \text{ m}^{-3}$; at $t = 6.5$, $(n_D + n_T) = 2.6 \times 10^{20} \text{ m}^{-3}$. Of this change, helium accumulation accounts for 79%; displacement by carbon accounts for the other 21%.

An often-used measure of the performance of a particular ignition sce-

nario is the product $\langle n_D + n_T \rangle \tau_E \langle T_i \rangle$, where τ_E is the global energy confinement time and $\langle T_i \rangle$ is the density-weighted, volume-averaged ion temperature. This parameter characterizes the balance between alpha power ($\propto \langle n_D n_T T_i^2 \rangle$) and the total losses ($\propto \langle n_D + n_T \rangle \langle T_i \rangle / \tau_E$, given that we can relate the hydrogenic ion energy to the total plasma energy by a constant factor). In simulation the Singer-Ku model simulation (I), we find that between $t = 6.5$ and $t = 9.0$ (when P_{net} , the time rate of change of the total plasma energy, first becomes negative), $\tau_E \langle T_i \rangle$ actually increases. However, this is more than offset by the decrease in hydrogenic ion density over the same time interval so that $\langle n_D + n_T \rangle \tau_E \langle T_i \rangle$ falls below the critical value for ignition.

The loss of deuterium and tritium also seems to be instrumental in ending the ignition in the Tang model simulation (II). In this case, $\Delta \langle n_D + n_T \rangle = -4.2 \times 10^{19} \text{ m}^{-3}$ between $t = 6.5$ and $t = 10.8$, with $\langle n_D + n_T \rangle = 2.9 \times 10^{20} \text{ m}^{-3}$ at $t = 6.5$. Helium ash buildup is responsible for 72% of the change; displacement by carbon accounts for the rest. The effects are smaller (the ignition ends more slowly) in this run due to the lower P_α and higher $\langle n_e \rangle$. Other effects that might be contributing to the termination of ignition in this case, and in our CIT simulations in general, will be described below.

We will now describe the conditions under which we expect the burnup of deuterium and tritium to be significant and then demonstrate what happens if the helium ash can be removed. This discussion can be better understood if we speak in terms of a 0-D power balance calculation (Plasma OPERATION CONtours or POPCON plots, see Refs. 8,9,38, and 40). We display the results of these computations as contours of constant P_{AUX} , the auxiliary power required to maintain steady state, in $\langle n_e \rangle$ vs. $\langle T_e \rangle$ space. For clarity, we show in Fig. 14 a "typical" POPCON plot for CIT using a τ_E scaling comparable to that obtained in the present simulations. More precise POPCONs for CIT have been given elsewhere.³⁸ Note that we can also loosely interpret P_{AUX} as the negative of the time rate of change of the total plasma energy (i.e., $-P_{net}$) in the absence of auxiliary power input. The $P_{AUX} = 0$ contour on the left side of the diagram represents ohmic equilibrium, while the one in the upper right corner denotes ignited equilibrium.

This POPCON plot is the result of solving

$$P_\alpha + P_{OH} + P_{AUX} = \frac{\frac{3}{2} \sum_j n_j T_j}{\tau_E} + P_{RAD}, \quad (14)$$

using a 0-D code,^{9,38,40} where P_α is the alpha power computed using prescribed profiles (parabolas with a user-specified exponent), P_{OH} is the ohmic heating power, P_{RAD} is the power loss due to bremsstrahlung radiation, the sum over j includes ions and electrons, and τ_E is calculated using some user-specified formula, for example Eq. (10). The equilibrium ignition contour goes to higher densities at the highest temperatures in part as a result of the effective exponent on T_i in the P_α formula falling below 2 when $T_i > 20$ keV.

When the electron density is held constant with no ash removal, ignited steady states at low density, but high temperature (so that the alpha power is significant) will be the most susceptible to deuterium - tritium burn up. In the POPCON plot, these conditions are represented by the lower right-hand portion of the ignited equilibrium contour.

Conversely, discharges with high density and low temperature (upper left of the ignited $P_{AUX} = 0$ contour) will be the least affected by helium ash accumulation. This is due not only to the higher density itself, but also to the lower P_α under these conditions. Furthermore, the effect of a given drop in density on P_{AUX} is smaller at very large densities. That is, the ignition contour in this case is given by the balance between P_α and $P_{RAD} \propto n_e^2 T_e^{1/2}$ so that there is no density dependence to the $P_{AUX} = 0$ contour.

We should point out that the left side of the ignited equilibrium contour is thermally unstable, $dP_{AUX}/d(T_e) < 0$.⁸ That is, a perturbation to the right will lead to a growing plasma energy; the resulting higher temperature raises $-P_{AUX}$ even more. This process would continue (if constant density were maintained) until $dP_{AUX}/d(T_e)$ changes sign (towards the right side of the ignited equilibrium contour). As a result, an ignited plasma with high density and low temperature would have to be held very close to the $P_{AUX} = 0$ contour to prevent such a runaway from creating higher P_α and significant deuterium - tritium burnup.

We now return to simulation I and consider the effects of removing the helium ash as it is formed. This is done by specifying a negative impurity influx. To get effective pumping we find it necessary to flatten the helium density profile by altering its diffusion model. Although this is not an experimentally realistic procedure, it does clearly show the impact the helium ash can have on CIT performance. The results of this simulation are depicted as the second P_α curve in Fig. 3. Note that the alpha power keeps increasing after ignition has ended in simulation I and appears to approach a steady

state near $t = 10.8$ sec. The total loss of deuterium and tritium between $t = 6.5$ and $t = 10.8$ is $\Delta\langle n_D + n_T \rangle = -1.1 \times 10^{19} \text{ m}^{-3}$; 91% of this is due to displacement by the influxed carbon atoms. In fact, $\langle n_D + n_T \rangle$ is very steady for $t > 8$ sec.

It is not completely clear why P_α does not continue to increase past 70 MW. If we again consider the product $\langle n_D + n_T \rangle \tau_E \langle T_i \rangle$, we find that now with $\langle n_D + n_T \rangle$ approximately constant and $\langle T_i \rangle$ increasing up to $t = 9$ sec, it is a drop in τ_E that causes the plasma conditions to stabilize. In particular, the conducted power seems to be increasing faster than $\langle T \rangle^2$. On the other hand, the central temperatures approach 30 keV in this run. At that level, the drop in P_α relative to $\langle n_D n_T T_i^2 \rangle$ could be important.

We can best explain the evolution of this simulation in terms of a POPCON diagram. The ratio $\langle n_D + n_T \rangle / \langle n_e \rangle$ is taken to be a constant over the entire $\langle n_e \rangle$ vs. $\langle T_e \rangle$ space. Varying the parameter representing this ratio leads to a family of $P_{AUX} = 0$ contours. If we instead imagine plotting the contours with an ordinate of $\langle n_D + n_T \rangle$, we can depict the trajectory of a discharge with time-varying deuterium and tritium density.

In the simulation with helium pumping, we find that after the auxiliary heating is turned off, P_{net} (i.e., $-P_{AUX}$) first increases with temperature and then falls. Near the end of the run, the plasma density, temperature, etc. approach steady values with $P_{net} < 1$ MW. On the POPCON plot, this means a trajectory starting (when the ICRF heating is completed) on the left side of the ignition region. It moves to the right with increasing temperature (going down slightly as the density drops a bit); in this way $-P_{AUX}$ rises, then falls. Finally, a stable steady state would be reached on the right side of the $P_{AUX} = 0$ contour (see Fig. 15).

So, it appears that the ignition contours predicted by BALDUR have the same shape as the ones in Fig. 14. However, the detailed values of P_{AUX} (or P_{net}) for a given density and temperature may not be the same (e.g., the 0-D code is not capable of modelling subtle transport effects). Even if the steady state is reached as a result of some transport-model-dependent feature, the details of the fusion cross section that give rise to the shape of the ignition contour in the POPCON diagram are real effects and likely would have led to a similar conclusion to the run (for the τ_E scaling used here).

In simulation I, the trajectory in $\langle n_D + n_T \rangle - \langle T_e \rangle$ space begins at the same point as the helium-pumped run following ICRF heating. The trajectory

again moves to the right, but it also moves down as the fuel is consumed. It continues in this way until the $P_{AUX} = 0$ contour is reached. Since P_{AUX} generally increases with decreasing density, there is no steady state here (fuel consumption continues). Hence, P_{AUX} becomes positive as the run continues so that the plasma loses energy, and the temperature drops until the discharge is terminated (see Fig. 15).

All of the effects described in this subsection are important in our simulations because the plasma conditions are so close to the bottom of the ignited $P_{AUX} = 0$ contour in the POPCON diagram of Fig. 15. If the plasma density were much higher or the energy confinement time scaling much more favorable, this would not be the case. Then, we would see an apparent thermal runaway for the (short) duration of a CIT discharge. We can also conclude here that control of the plasma density is one suitable method of burn control. That is, if the density rises uncontrollably, we might end up with a real runaway discharge.

We now mention briefly other effects that have had an impact on the burn phase of these and previous simulations. Perhaps most important is the broadening of the sawtooth mixing radius with time (see Fig. 13). The resulting flattening of the profiles leads to a decreasing alpha power even if the deuterium - tritium density is maintained. These effects are even greater if ballooning-enhanced transport is included.

Two subtler phenomena could affect a very marginal discharge. The first of these involves the radiation increase that follows the inward diffusion of the carbon influxed during the burn phase. Since most of the radiation in these simulations is due to bremsstrahlung, this rise is just a result of a higher Z_{eff} in the hot plasma core. Finally, in cases with large amounts of helium pumping, the deuterium - tritium gas puffing required to maintain constant electron density can be significant. This leads to a higher neutral density near the edge and, consequently, to increased charge exchange losses.

IV. Sensitivity to Assumptions

In this section we will discuss briefly how our results depend on: (i) whether or not the profiles are constrained to be nearly stable with respect to high- n ballooning modes, (ii) the shape of the heating profile, (iii) inclusion of the bootstrap current, and (iv) the particle transport model. This list of

topics is intended to complement the sensitivity tests performed in Ref. 10.

A. Ballooning Modes

Simulation I as described above includes the ballooning-enhanced transport.⁹ Removing the enhancement leads to very little difference in the results. The profiles do not show much effect due to the relatively small sawtooth mixing radius. The peak values become $\beta = 4.5\%$ and $P_\alpha = 71\text{MW}$; both are slightly higher than in the original run ($\beta = 3.8\%$, $P_\alpha = 60\text{MW}$). Furthermore, the ignition phase develops and ends in the same manner as discussed in Sec. III.A. The only quantities exhibiting any significant change are the central temperatures; without the ballooning-enhanced transport, they can peak up at the end of each sawtooth rise (e.g., as in Fig. 10).

As noted previously, simulation II does not include the ballooning-enhanced transport. Due to the broad sawtooth oscillations, enforcing ballooning stability has a great effect on the outcome of the calculation. When this is done, the central temperatures remain essentially flat out to the mixing radius throughout each sawtooth rise. The resulting decrease in fusion power leads to much poorer performance. The simulation with ballooning mode-enhanced transport does ignite, but only for a fraction of a second. We find peak parameters well below those of simulation II: $\beta = 1.8\%$ and $P_\alpha = 22\text{MW}$.

From these runs, we conclude that the consequences of enforcing ballooning-stable profiles depend greatly on the size of the sawtooth mixing radius. Furthermore, due to the fact that the modes are typically unstable only inside of the mixing radius (with a critical pressure gradient of almost zero), the effects of the ballooning-enhanced transport are almost equivalent to greatly reducing the sawtooth period.

Many of the assumptions made in deriving the ideal MHD ballooning mode equation⁹ do not strictly hold in an ignited CIT. In particular, the large, central, low-shear region and nonthermal alpha particles are not allowed for in the orderings leading to it. The appropriate calculations are far too complicated to be included as part of the BALDUR simulations. Instead, we transfer information about the equilibrium profiles to other groups to be analyzed in a more rigorous fashion.

The PEST stability code has been used to analyze the data from simulation I.⁴¹ In addition to looking at high-n ballooning and Mercier modes, this

code considers low- n , pressure-driven modes in the low shear limit (infernal modes⁴²) and external kinks. The low shear region inside of the sawtooth mixing radius in simulation I is predicted to be unstable with respect to Mercier and other pressure-driven modes, but is otherwise stable. Instability is predicted in the center despite the activity of the ballooning-enhanced thermal transport in part because of the absence of ballooning-enhanced particle transport in our model. The peaking of the density profile during the sawtooth rise due to the inward pinch leads to a small, but non-zero pressure gradient.

Rewoldt has investigated the effects of the high-energy alpha particles on high- n instabilities.⁴³ The data used were taken at $t = 9$ sec from a preliminary run qualitatively similar to simulation I. The calculation was performed on a flux surface near $r/a = 0.5$. He found that the alpha particles have a weak effect on the trapped electron drift mode, but substantially lowered the critical β for the kinetically calculated MHD ballooning mode. In fact, this ballooning mode was predicted to be unstable for the parameters used. The thermalized helium ash does little to alter the behavior of either instability.

B. Heating Profile

The width (and location of the peak) of the ICRF deposition profile can affect the energy confinement time. As was discussed in Sec. III.A, τ_E actually rises in simulation I with the onset of auxiliary heating; this is in part the result of the narrow deposition profile used. We have tried broader heating profiles not only to verify that this explanation is reasonable but also to determine how important these effects are to CIT performance. Thus far, we have only looked at simulations involving the Singer-Ku transport model.

We find that if the heating profile is broad enough (for example, dropping to half of its central value by $r = 0.4$ m), the confinement time does fall when the auxiliary heating is turned on and remains lower than in the case with a narrow profile (ignoring the effects of pellets). Depending on how peaked the heating is, CIT may require more time or auxiliary power to reach ignition temperatures. Both simulations I and II show $P_{net} > 0$ when the auxiliary power is turned off. That is, they would actually ignite at lower temperatures. So, there is some room for a broader profile even within the present scenarios.

Previous simulations of CIT using the BALDUR code¹⁰ have shown that the location of the peak affects performance; a centrally peaked profile is most desirable. In that a profile peaking off-axis deposits more power closer to the edge, their results are consistent with our conclusions regarding the width of the heating profile. We would also like to point out that there is now some evidence in experimental data for the shapes of heating profiles affecting the energy confinement time.⁴⁴

The alpha-heating model used in the above simulations does not allow sawtooth mixing of the high energy alpha particles. It is not certain from a theoretical standpoint whether or not this mixing should occur in an actual experiment. In order to determine if it matters, we now describe the results of a simulation using a simpler alpha-heating model¹¹ that does allow mixing of the slowing-down particles. The run used for the comparison is simulation II; the broad sawtooth oscillations should nearly maximize the effect. However, we find that the various temperatures and β values vary between the two runs by only a few percent or less; the peak alpha power is $P_\alpha = 43$ MW, much as it is in simulation II. Furthermore, the details of the evolution of the burn phase are virtually unaltered.

We might have expected some effect from this procedure due to the alterations in the effective alpha-heating profile. The reason we do not may have to do with the fact that all of the changes are taking place inside of the sawtooth mixing radius. The confinement of the bulk plasma energy within this region is largely governed by the sawtooth oscillations, so that varying the heating profile here produces only negligible effects.

C. Bootstrap Current

We consider two runs: one with the bootstrap current and one without. Simulation I serves as the former, and the fast ramp case used in the discussion of Sec. III.B will be the latter. As described in Refs. 9 and 31, the bootstrap current, J_{boot} , is proportional to a sum of density and temperature gradients and vanishes at the magnetic axis. Hence, J_{boot} peaks off-axis. In simulation I, the peak occurs just outside of the sawtooth mixing radius; the bootstrap current accounts for approximately 20% of the total current at this radius during the burn phase. With the profiles in use here, J_{boot} falls more slowly with r than the total current density; it is never so large that the

loop voltage becomes negative. Thus, it is not too surprising that we find the total current profile in the case without bootstrap current to be slightly more peaked than in simulation I. This gives rise to the approximately 0.04 m increase in the mixing radius from the value quoted in Sec. III.B (~ 0.14 m) to that shown in Fig. 13. We also note that the bootstrap current tends to smooth out the current profile; there is otherwise a ledge just outside of the mixing radius [see Fig. 11(b)].

Although the bootstrap current appears to be of limited importance in CIT, it need not be in other reactor designs. There may be more interest in this neoclassical effect since there is now experimental evidence of its existence.³

D. Particle Transport Model

The main impact of the particle transport model in CIT is on the density profile during the burn phase. In particular, the shape of the density profile is determined by the ratio v/D [see Eq. (6)]. This effect enters through the alpha power which increases roughly with the square of the central density (see Sec. III.B). So in general, the fusion power can be altered either by changing the volume-averaged density (Fig. 14) or by forcing the density profile to have a different shape with the same volume average.²² If it turns out that the density profiles in CIT are flat (as they are in a typical H-mode), the performance might be degraded considerably from what is described in this paper. This concern motivated in part the inclusion here of simulation II. Its broad sawteeth lead to a flat density profile despite the presence of the inward pinch; the effects of the relatively low central density are apparent in Fig. 4. In general, a flat density profile requires a higher volume-averaged density or better energy confinement to achieve the same performance level as a discharge with a peaked profile. If CIT does exhibit flat density profiles, it will likely need to be operated at or above the most conservative estimates of the density limit (see Sec. II.A) in order to reach ignition.

V. Conclusions

In this paper, we have presented detailed 1-1/2-D transport simulations of CIT that include time variations of fields, densities and plasma shape,

as well as various MHD and neoclassical effects. Two thermal transport models are employed; both are constrained to yield a scaling for the global energy confinement time that is better than L-mode [as defined by Eq. (10)]. The temperature profiles from the two simulations differ significantly due to the dissimilar sawtooth oscillation widths. The responses in τ_E in each case to transients such as pellet injection and the initiation of auxiliary heating are not the same. Yet, both simulations result in an ignition period of at least two seconds. The run with the broader sawtooth oscillations requires a somewhat higher density to allow ignition to be achieved.

From these simulations, previous unpublished simulations and various 0-D calculations, we conclude that CIT should ignite if a confinement scaling of $\tau_E/\tau_{E,KG} \simeq 1.4$ can be maintained at power levels up to 60 MW.

That broad sawtooth oscillations can hinder reactor performance has been suggested previously.^{9,22} The long resistive skin time in CIT compared with the length of the discharge means that the sawtooth mixing radius during the burn phase depends on how the current is loaded during the start-up. We contrasted three different start-up scenarios (Sec. III.B) using the Singer-Ku transport model²³ to demonstrate this point. In particular, it appears that in CIT avoiding skin currents requires both magnetic field and plasma shape ramps. At the same time, preventing broad sawtooth oscillations (and disruptions) constrains q_{cyl} from dropping too low during this period. The optimum scheme may be one in which q_{cyl} falls monotonically in time from its initial value with a circular cross-sectional plasma to its final state with an elongated cross section.

After studying the burn phases of the discharges presented here, we conclude that if the volume-averaged electron density is held fixed and helium ash not removed, ignition ends due to the drop in deuterium - tritium density. This is demonstrated in Fig. 3 where we show a simulation in which helium is pumped as it is formed; in this case, a nearly steady-state ignition is achieved by the end of the run. The alpha power remains reasonable because CIT does not have a great deal of ignition margin at these parameters.

It is clear from this work that control of the deuterium and tritium densities is equivalent to burn control. On the one hand, if the fuel densities cannot be maintained, ignition will cease. On the other, if the plasma density cannot be restrained, the plasma will likely run away.

The primary concern of future work should be the development of more re-

liable transport models and scaling laws; this is also the conclusion of Singer, et al. in Ref. 10. Although we have relied here on the Kaye-Goldston scaling law for our reference L-mode energy confinement time (Eq. (10)), there are others that are not nearly as favorable for CIT.^{25,45} As was noted above, CIT will need to do even better than Kaye-Goldston L-mode in order to ignite. So, schemes for enhanced confinement operation are also needed. Transport models for the H-mode are currently being developed.⁴⁸ Newer ways of enhancing confinement have been recently discovered^{3,47}; their applicability to CIT is uncertain, however.

The above-stated requirements on the energy confinement time can be relaxed somewhat if the electron density is allowed to exceed the values used here (see Sec. II.A). Fortunately, there is now some evidence, given by Greenwald, that this is reasonable.¹⁹ On the other hand, more work is needed to widen the experimental data base for the Greenwald scaling and to provide theoretical explanations and transport models (see, for example, Ref. 48). Even if densities higher than $3 \times 10^{20} \text{ m}^{-3}$ are possible, there is some concern with the fuelling of the device at that level.¹⁹ It is likely that a reliable pellet injector capable of significant penetration (during at least the low temperature phase of the discharge) will be required.

Acknowledgement

This work was supported by U.S. DOE Contract No. DE-AC02-76-CHO-3073.

References

- ¹D. POST, W. HOULBERG, G. BATEMAN et al., "Physics Aspects of the Compact Ignition Tokamak," *Physica Scripta* **T16**, 89 (1987).
- ²J. LUXON, P. ANDERSON, F. BATTY, C. BAXI, G. BRAMSON, et al., "Initial Results for the DIII-D Tokamak," *Proc. 11th Int. Conf. Plasma Physics and Controlled Nuclear Fusion*, Kyoto, Japan, November 13-20, 1986, p. 159, IAEA-CN-47/A-III-3, International Atomic Energy Agency.
- ³R. J. HAWRYLUK, V. ARUNASALAM, M. G. BELL, M. BITTER, W. R. BLANCHARD, et al., "TFTR Plasma Regimes," *Proc. 11th Int. Conf. Plasma Physics and Controlled Nuclear Fusion*, Kyoto, Japan, November 13-20, 1986, p. 51, IAEA-CN-47/A-I-3, International Atomic Energy Agency.
- ⁴JET Team: H. ALTMANN, R. J. ANDERSON, J. ARBEZ, W. BAILEY, D. V. BARTLETT, et al., "JET Latest Results and Future Prospects," *Proc. 11th Int. Conf. Plasma Physics and Controlled Nuclear Fusion*, Kyoto, Japan, November 13-20, 1986, p. 31, IAEA-CN-47/A-I-2, International Atomic Energy Agency.
- ⁵M. H. REDI, W. M. TANG, P. C. EFTHIMION, D. R. MIKKELSEN, and G. L. SCHMIDT, "Transport Simulations of Ohmic TFTR Experiments with Microinstability Based Profile Consistent Models for Electron and Ion Thermal Transport," *Nucl. Fusion* **27**, 2001 (1987).
- ⁶R. R. DOMINGUEZ and R. E. WALTZ, "Tokamak Transport Code Simulations with Drift Wave Models," *Nucl. Fusion* **27**, 65 (1987).
- ⁷R. J. GOLDSTON, "Topics in Confinement Analysis of Tokamaks with Auxiliary Heating," *Proc. Course and Workshop Basic Physical Processes of Toroidal Fusion Plasmas*, Varenna, Italy, August 26 - September 3, 1985, p. 165, EUR-10418-EN, CEC, Brussels.
- ⁸W. A. HOULBERG, S. E. ATTENBERGER, and L. M. HIVELY, "Contour Analysis of Fusion Reactor Plasma Performance," *Nucl. Fusion* **22**, 935 (1982).

- ⁹D. P. STOTLER, D. POST, and G. BATEMAN, "Sawtooth Effects in INTOR and TIBER." PPPL-2463, Princeton Plasma Physics Laboratory (1987). (submitted for publication in *Fusion Technology*).
- ¹⁰C. E. SINGER, G. BATEMAN, and L. P. KU, "Plasma Transport in a Compact Ignition Experiment," PPPL-2414, Princeton Plasma Physics Laboratory (1987) (submitted for publication in *Fusion Technology*).
- ¹¹C. SINGER, D. POST, D. MIKKELSEN, M. REDI, A. MCKENNEY, A. SILVERMAN, F. SEIDL, P. RUTHERFORD, R. HAWRYLUK, W. LANGER, L. FOOTE, D. HEIFETZ, W. HOULBERG, M. HUGHES, R. JENSEN, G. LISTER, and J. OGDEN, "BALDUR: A One-Dimensional Plasma Transport Code," PPPL-2073, Princeton Plasma Physics Laboratory (1986) (to appear in *Computer Physics Communications*).
- ¹²G. BATEMAN, "Algorithms for 1-1/2-D Transport," in *Proceedings of the 1985 Trieste Spring College on Plasma Physics* (to be published).
- ¹³F. WAGNER, G. BECKER, K. BEHRINGER, D. CAMPBELL, A. EBERHAGEN, et al., "Regime of Improved Confinement and High Beta in Neutral-Beam-Heated Divertor Discharges of the ASDEX Tokamak," *Phys. Rev. Lett.* **49**, 1408 (1982).
- ¹⁴J. C. DeBOO, "Confinement Studies in DIII-D," *Bull. Am. Phys. Soc.* **32**, 1711 (1987).
- ¹⁵S. M. KAYE and R. J. GOLDSTON, "Global Energy Confinement Scaling for Neutral-Beam-Heated Tokamaks," *Nucl. Fusion* **25**, 65 (1985).
- ¹⁶N. POMPHREY, S. C. JARDIN, and J. MANICKAM, "One Complete Discharge in the Compact Ignition Tokamak," *Bull. Am. Phys. Soc.* **32**, 1982 (1987).
- ¹⁷M. MURAKAMI, J. D. CALLEN, and L. A. BERRY, "Some Observations on Maximum Densities in Tokamak Experiments," *Nucl. Fusion* **16**, 347 (1976).
- ¹⁸K. B. AXON, W. H. M. CLARK, J. G. CORDEY, M. COX, S. J. FIELDING, et al., "Beam-Driven Currents, Power Balances and Density Limits with Neutral Injection into DITE," *Proc. 8th Int. Conf. Plasma Physics*

- and *Controlled Nuclear Fusion*, Brussels, Belgium, July 1-10, 1980, p. 413. IAEA-CN-38/N-4, International Atomic Energy Agency.
- ¹⁹M. GREENWALD, M. BESEN, F. CAMACHO, C. FIORE, M. FOORD, et al., "Studies of the Regime of Improved Particle and Energy Confinement following Pellet Injection into Alcator C," *Proc. 11th Int. Conf. Plasma Physics and Controlled Nuclear Fusion*, Kyoto, Japan, November 13-20, 1986. p. 139, IAEA-CN-47/A-III-1, International Atomic Energy Agency.
- ²⁰F. H. SEGUIN, R. PETRASSO, and E. S. MARMAR, "Effects of Internal Disruptions on Impurity Transport in Tokamaks," *Phys. Rev. Lett.* **51**, 455 (1983).
- ²¹M. GREENWALD, D. GWINN, S. MILORA, J. PARKER, R. PARKER, et al., "Pellet Fuelling Experiments in Alcator-C," *Proc. 10th Int. Conf. Plasma Physics and Controlled Nuclear Fusion*, London, U.K., September 12-19, 1984, p. 45, IAEA-CN-44/A-I-3, International Atomic Energy Agency.
- ²²G. BATEMAN, "Delaying Sawtooth Oscillations in the Compact Ignition Tokamak," PPPL-2373, Princeton Plasma Physics Laboratory (1986) (to appear in *Fusion Technology*).
- ²³C. SINGER, L.-P. KU, G. BATEMAN, F. SEIDL, and M. SUGIHARA, "Physics of Compact Ignition Tokamak Designs," *Proc. 11th Symp. Fusion Engineering*, Austin, Texas, November 18-22, 1985, p. 41.
- ²⁴C. S. CHANG and F. L. HINTON, "Effect of Finite Aspect Ratio on the Neoclassical Ion Thermal Conductivity in the Banana Regime," *Phys. Fluids* **25**, 1493 (1982).
- ²⁵R. J. GOLDSTON, "Energy Confinement Scaling in Tokamaks: Some Implications of Recent Experiments with Ohmic and Strong Auxiliary Heating," *Plasma Phys. Controlled Fusion* **26**, 87 (1984).
- ²⁶M. KEILHACKER, G. BECKER, K. BERNHARDI, A. EBERHAGEN, M. EISHAER, et al., "Confinement Studies in L and H-Type ASDEX Discharges," *Plasma Phys. Controlled Fusion* **26**, 49 (1984).

- ²⁷N. A. UCKAN, W. A. HOULBERG, and J. SHEFFIELD, "Physics Evaluation of Compact Tokamak Ignition Experiments," *Proceedings 11th Symp. Fusion Engineering*, Austin, Texas, November 18-22, 1985, p. 401.
- ²⁸B. B. KADOMTSEV, "Disruptive Instabilities in Tokamaks," *Sov. J. Plasma Phys.* **1**, 389 (1975).
- ²⁹J. W. CONNOR, J. B. TAYLOR, and M. F. TURNER, "Ideal MHD Ballooning Instability and Scaling Law for Confinement," *Nucl. Fusion* **24**, 642 (1984).
- ³⁰M. AZUMI, T. TSUMENATSU, K. ITOH, T. TUDA, G. KURITA, et al., "Evolution of Stable High-Beta Tokamak Equilibria," *Proc. 8th Int. Conf. Plasma Physics and Controlled Nuclear Fusion*, Brussels, Belgium, July 1-10, 1980, p. 293, IAEA-CN-38/K-1-1, International Atomic Energy Agency.
- ³¹S. P. HIRSHMAN and D. J. SIGMAR, "Neoclassical Transport of Impurities in Tokamak Plasmas," *Nucl. Fusion* **21**, 1079 (1981).
- ³²S. P. HIRSHMAN, "Neoclassical Current in a Toroidally-Confined Multi-species Plasma," *Phys. Fluids* **21**, 1295 (1978).
- ³³D. P. STOTLER, G. BATEMAN, and M. H. REDI, "Transport Simulations of the Compact Ignition Tokamak," Sherwood Theory Meeting, San Diego, California, 1987, paper 2D28.
- ³⁴P. COLESTOCK, Princeton Plasma Physics Laboratory, private communication.
- ³⁵C. K. PHILLIPS, Princeton Plasma Physics Laboratory, private communication.
- ³⁶A. SYKES, M. F. TURNER, and S. PATEL, "Beta Limits in Tokamaks Due to High-n Ballooning Modes," *Proc. 11th European Conf. Controlled Fusion and Plasma Physics*, Aachen, FRG, September 5-9, 1983, p. 363, European Physical Society. in *Controlled Fusion and Plasma Physics*, (11th European Conference, Aachen, European Physical Society), Vol. 7D, Part II, 363 (1983).

- ³⁷F. TROYON, T. GRUBER, H. SAUREMANN, S. SEMENZATO, S. SUCCI, "MHD-Limits to Plasma Confinement," *Plasma Phys. Controlled Fusion* **26**, 209 (1984).
- ³⁸Y. C. SUN, D. E. POST, G. BATEMAN, and D. STOTLER, "Power Balance Calculations for CIT and Ignition Designs," *Bull. Am. Phys. Soc.* **32**, 1921 (1987).
- ³⁹C. Z. CHENG, H. P. FURTH, and A. H. BOOZER, "MHD Stable Regime of the Tokamak," *Plasma Phys. Controlled Fusion* **29**, 351 (1987).
- ⁴⁰N. A. UCKAN and J. SHEFFIELD, "A Simple Procedure for Establishing Ignition Conditions in Tokamaks," in *Tokamak Startup - Problems and Scenarios Related to the Transient Phases of Ignited Tokamak Operation* (Plenum, New York, 1986), 45.
- ⁴¹M. W. PHILLIPS, Grumman Space Systems Division, private communication.
- ⁴²J. MANICKAM, N. POMPHREY, and A. M. M. TODD, "Ideal MHD Stability Properties of Pressure-Driven Modes in Low Shear Tokamaks," *Nucl. Fusion* **27**, 1461 (1987).
- ⁴³G. REWOLDT, " α -Particle Effects on High-n Instabilities in Tokamaks," *Bull. Am. Phys. Soc.* **32**, 1771 (1987).
- ⁴⁴J. D. CALLEN, J. P. CHRISTIANSEN, J. G. CORDEY, P. R. THOMAS and K. THOMSEN, "Modelling of Temperature Profiles and Transport Scaling in Auxiliary Heated Tokamaks," *Nucl. Fusion* **27**, 1857 (1987).
- ⁴⁵Y. SHIMOMURA and K. ODAJIMA, "Empirical Scaling of Incremental Energy Confinement Time of L-Mode Plasma and Comments on Improved Confinement in Tokamaks," *Comments on Plasma Physics and Controlled Fusion* **10**, 207 (1987).
- ⁴⁶C. E. SINGER, G. BATEMAN, and D. P. STOTLER, "Boundary Conditions for H-Mode Simulations in Tokamaks," *Bull. Am. Phys. Soc.* **32**, 1917 (1987).

⁴⁷JET Team, "Latest Results from JET," *Bull. Am. Phys. Soc.* **32**, 1711 (1987).

⁴⁸D. P. STOTLER and G. BATEMAN, "Simulations of a Density Limit in Radiation-Dominated Tokamak Discharges," *Bull. Am. Phys. Soc.* **32**, 1918 (1987).

major radius (m)	R_0	1.75
minor radius (m)	a	0.55
elongation	κ	2.0
triangularity	δ	0.4
toroidal field (T)	B_T	10.0
plasma current (MA)	I_p	9.0

Table 1: Flat-top parameters for CIT

Figures

- FIG. 1. Time dependence of various specified discharge parameters; units are given separately with each.
- FIG. 2. Contours of constant toroidal flux at various times for the fast ramp case discussed in Sec. III.B (similar to simulation I).
- FIG. 3. Time dependence of the ohmic, auxiliary, and alpha power for simulation I (solid line). The dashed line represents a simulation in which helium ash is pumped out during the flat-top.
- FIG. 4. Time dependence of the ohmic, auxiliary, and alpha power for simulation II.
- FIG. 5. β due to fast alpha particles in simulation I as a function of time and plasma half-width.
- FIG. 6. Global energy confinement time as a function of time for simulations I (dashed line) and II (solid line). The arrows indicate the times of pellet injection.
- FIG. 7. Electron density as a function of radial half-width and time for simulation I.
- FIG. 8. Electron density as a function of radial half-width and time for simulation II.
- FIG. 9. Ion temperature as a function of radial half-width and time for simulation I.
- FIG. 10. Ion temperature as a function of radial half-width and time for simulation II.
- FIG. 11. Current density as a function of radial half-width for four different simulations at (a) $t = 3$. and (b) $t = 7$. sec. Curves for the three different ramp schemes discussed in Sec. III.B and for simulation II are shown.
- FIG. 12. Time evolution of q_{cm} for three different plasma shape ramp schemes. The line patterns are as in Fig. 11; simulation II follows the same path as the fast ramp scheme.

FIG. 13. Time evolution of the sawtooth mixing radius for three different plasma shape ramp schemes and simulation II. The line patterns are as in Fig. 11. There are no sawteeth between $t \simeq 1.5$ sec and $t \simeq 8$ sec for the fixed shape case.

FIG. 14. Typical plot of the contours of auxiliary power (solid lines) required to maintain steady state in CIT as a function of $\langle n_e \rangle$ and $\langle T_e \rangle$. We indicate also contours of constant P_α (dashed lines).

FIG. 15. Trajectories for simulation I without ash removal (solid circles) and with ash removal (open circles) in hydrogenic density vs. ion temperature space. Heuristic curves for the ignited equilibrium ($P_{net} = 0$) and marginal thermal stability contours ($dP_{net}/\langle T_i \rangle = 0$) are included to allow a qualitative comparison with Fig. 14. The contours are drawn so as to be consistent with the data from the two runs.

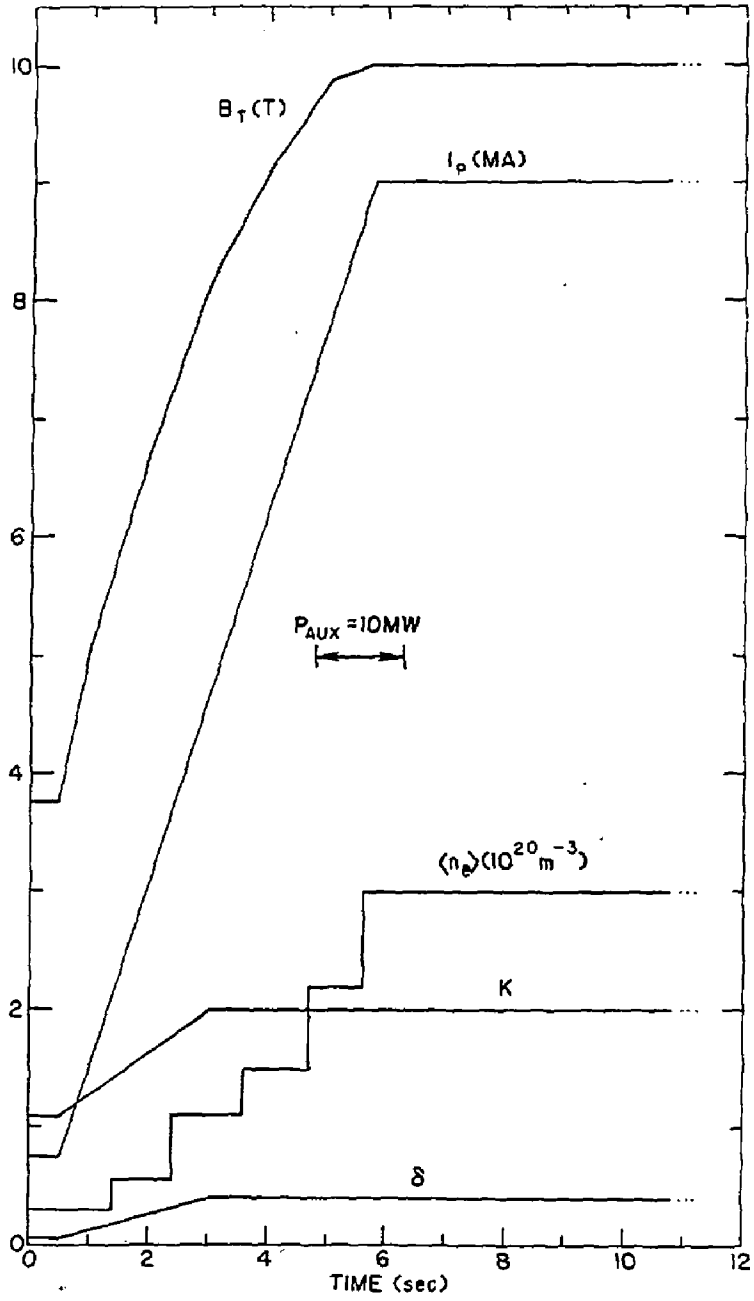


Fig. 1

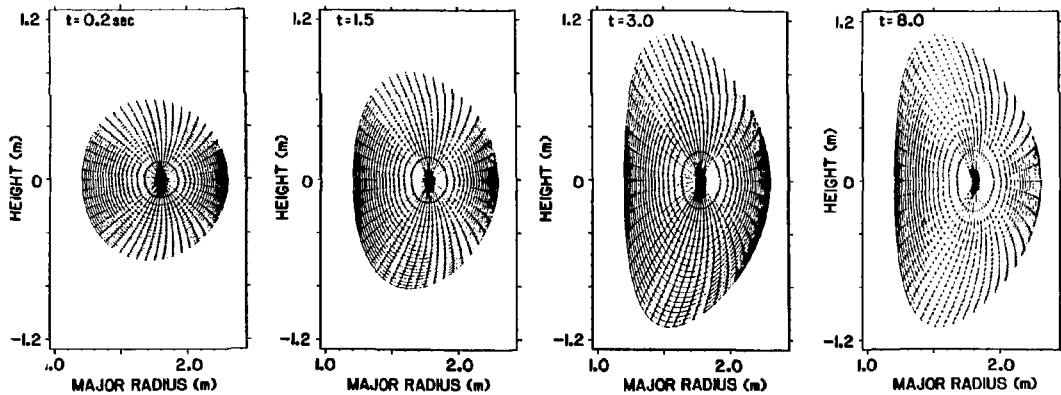


Fig. 2

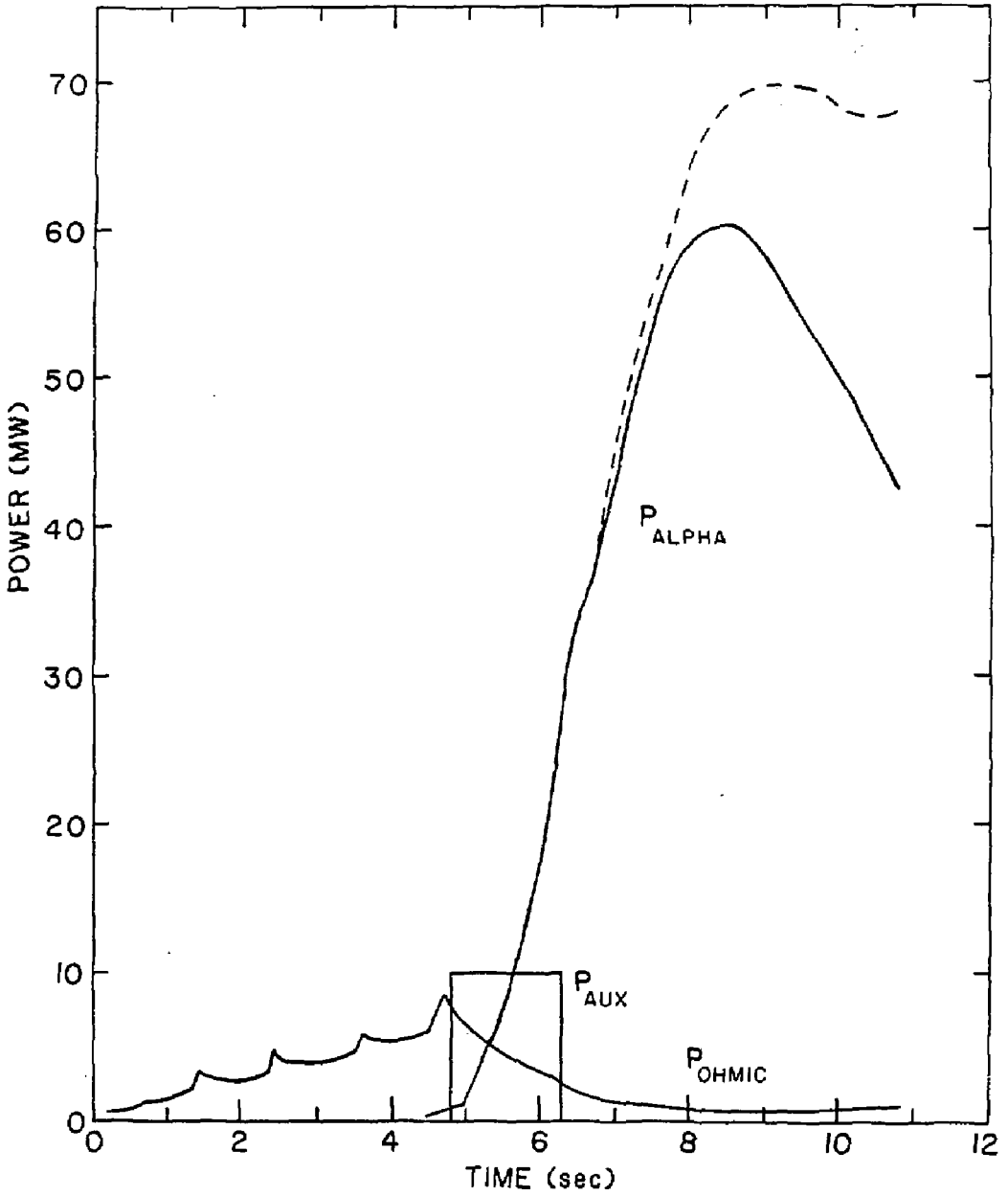
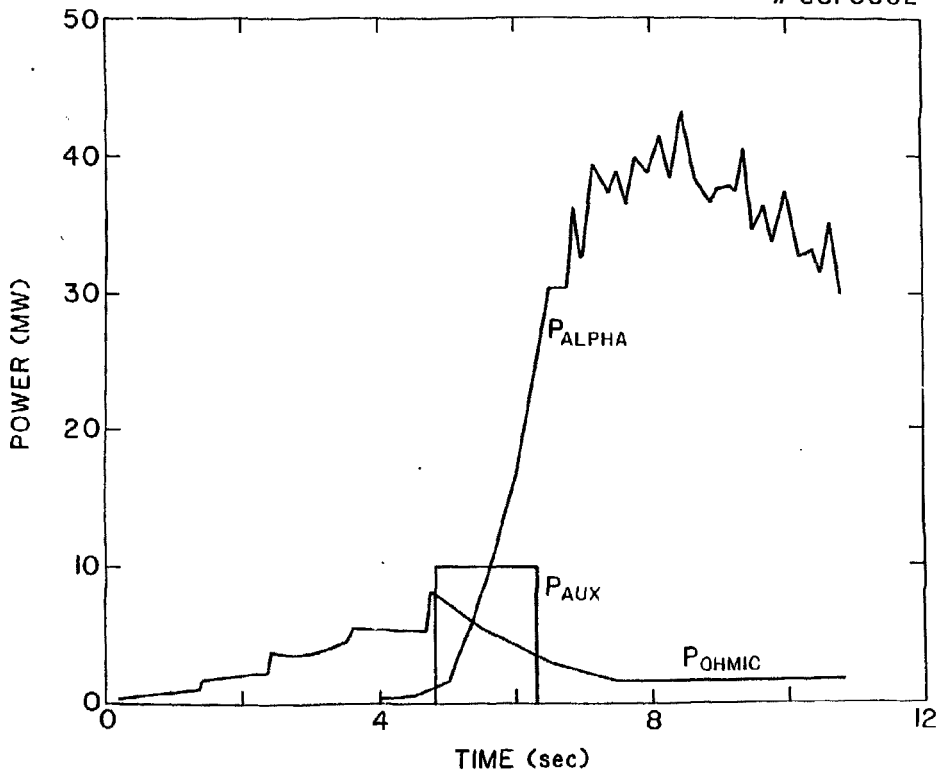


Fig. 3

#88P0032



#88P0033

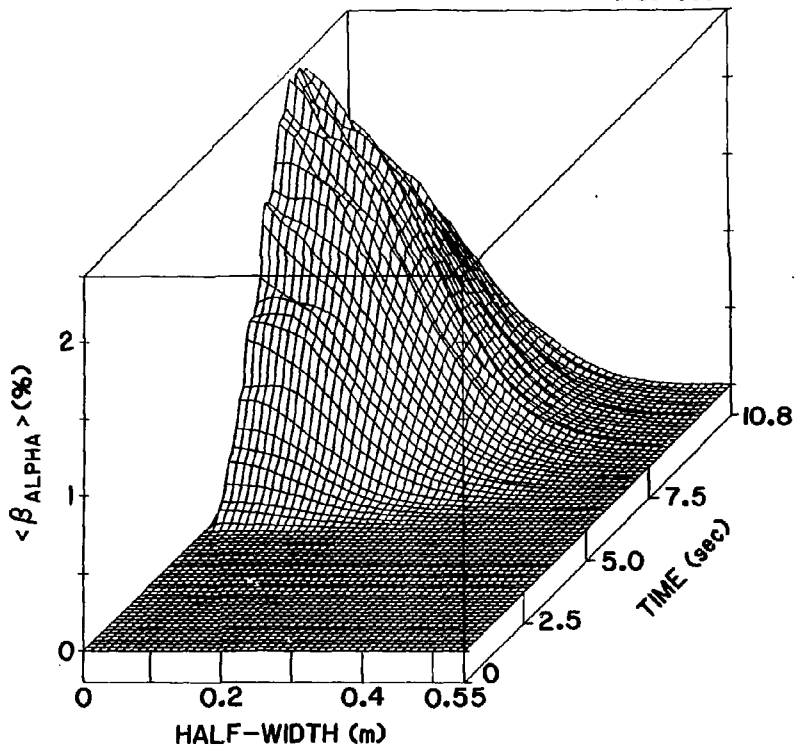


Fig. 5

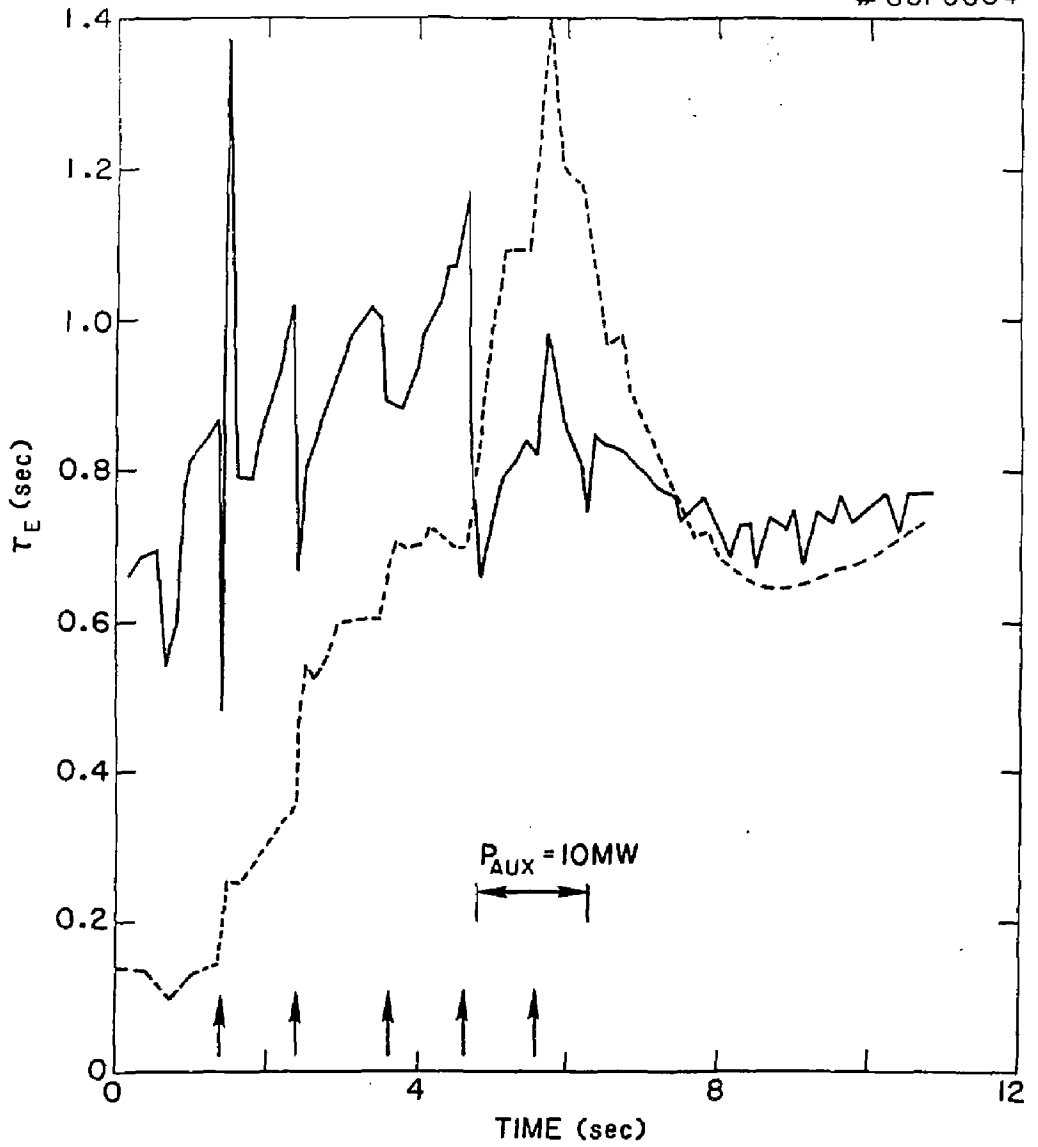


Fig. 6

#87P0157

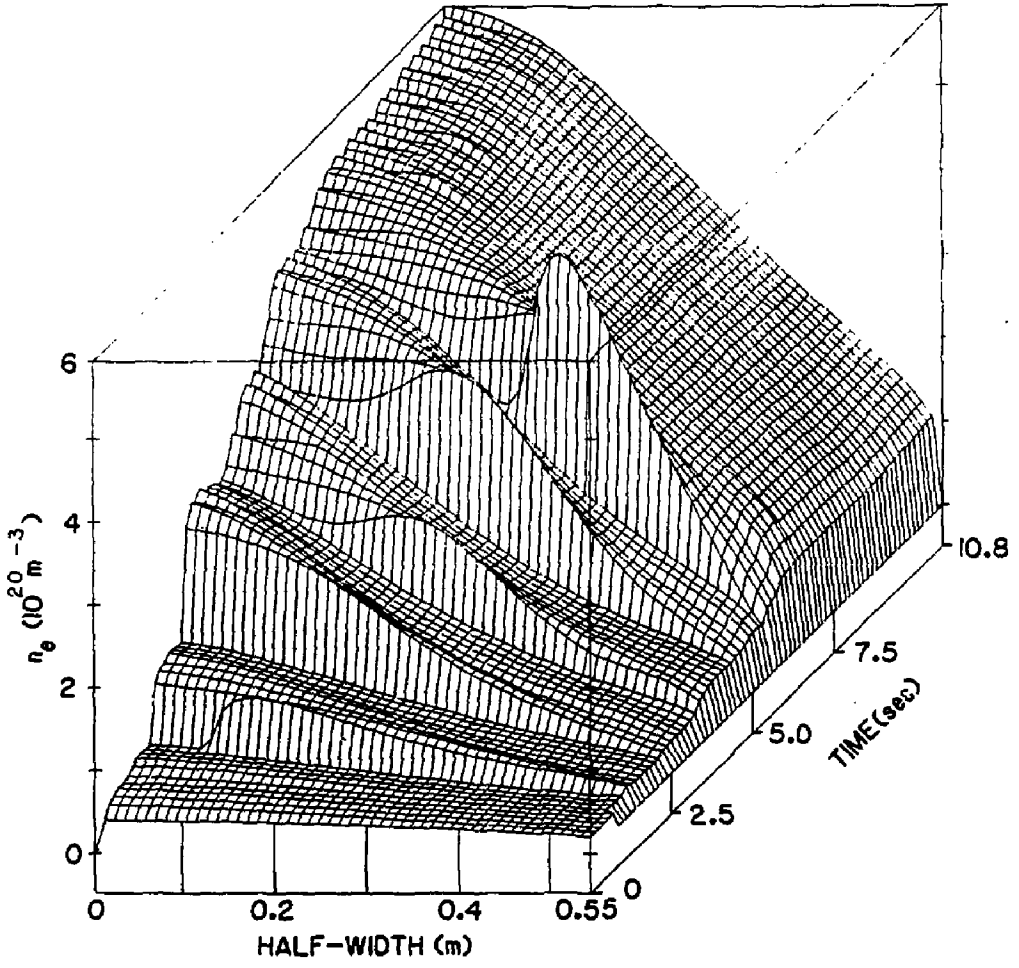


Fig. 7

#87PO158

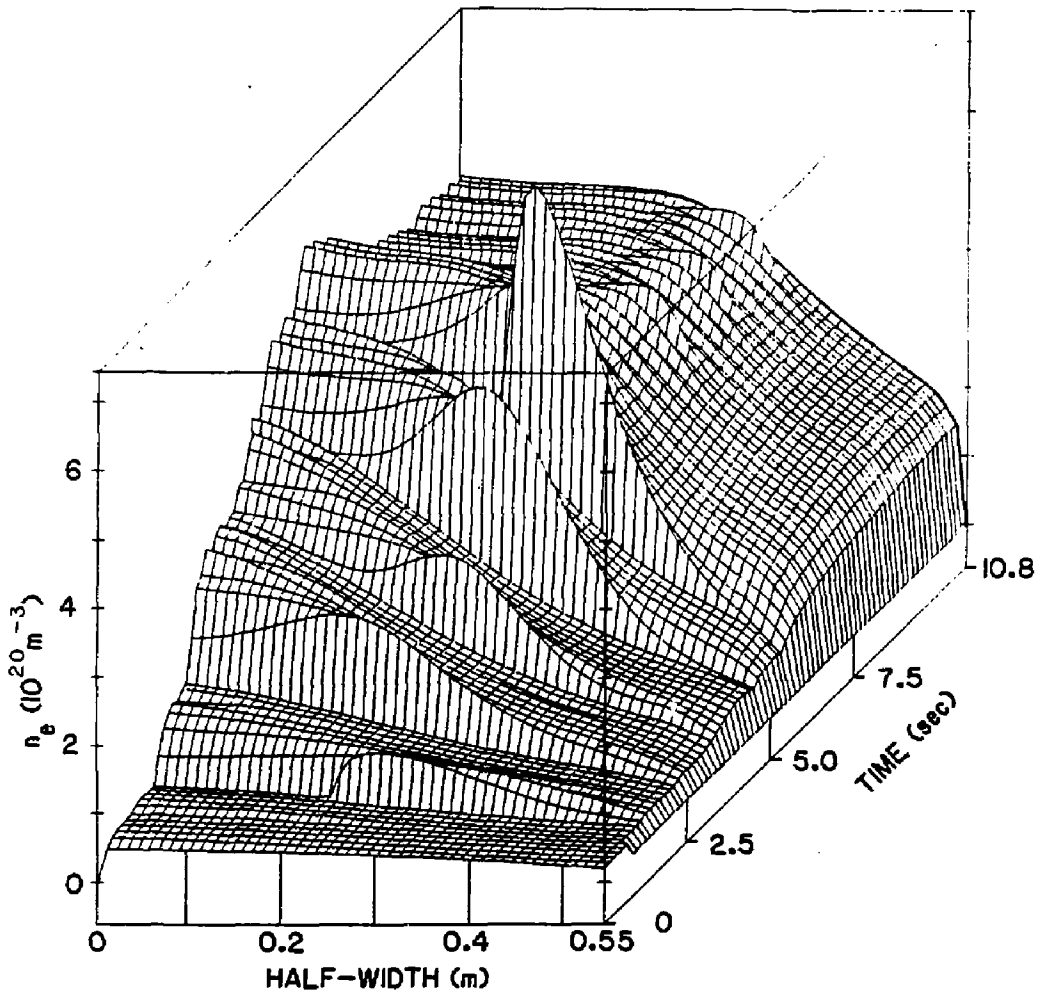


Fig. 8

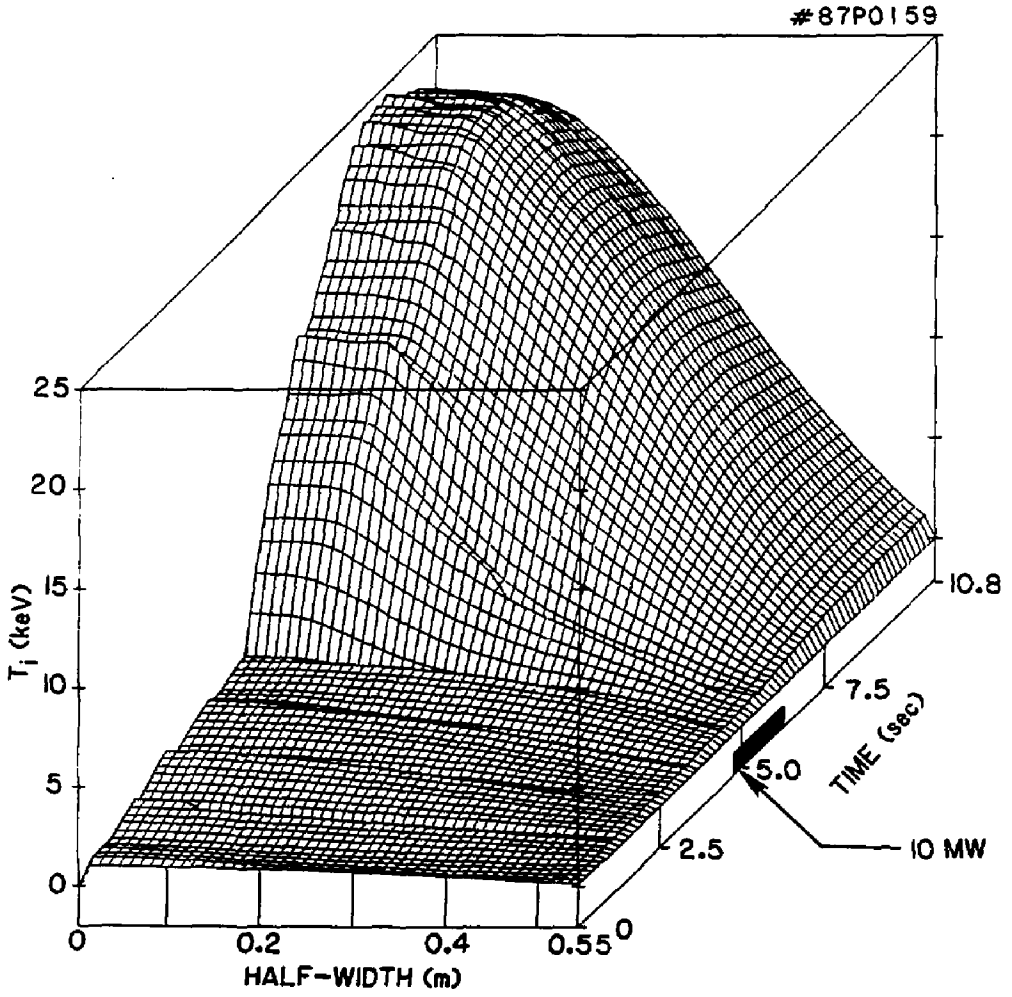


Fig. 9

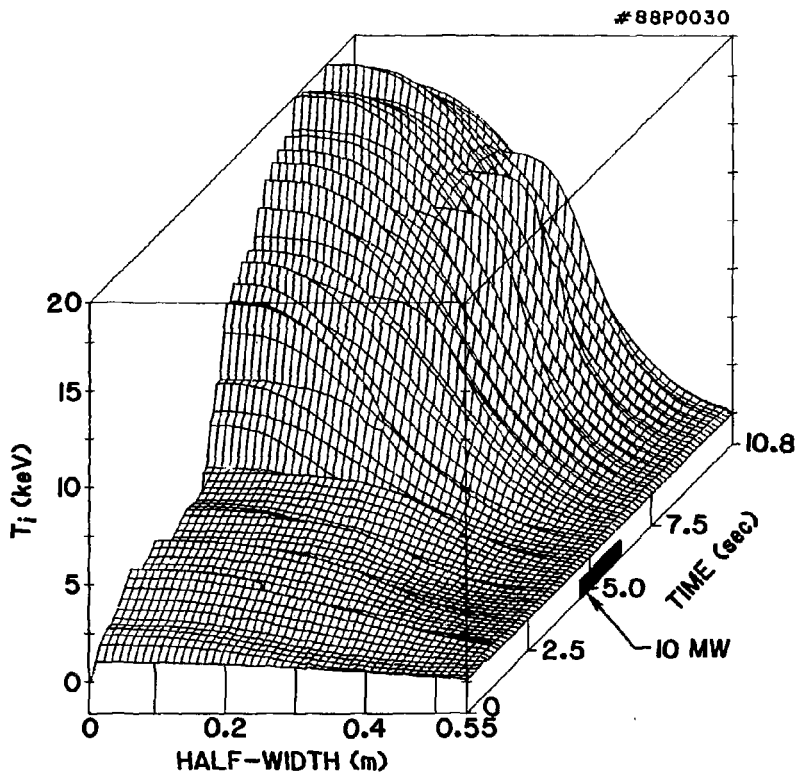


Fig. 10

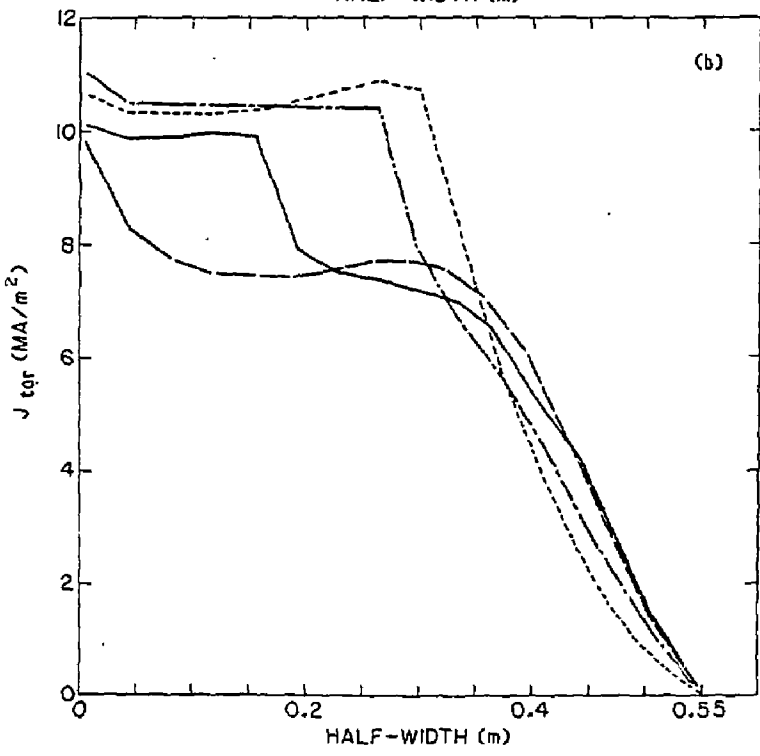
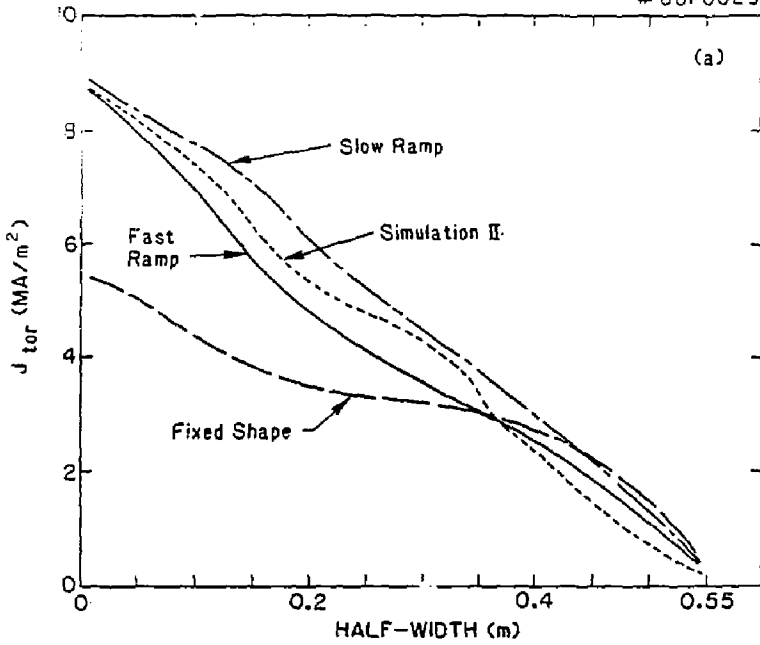


Fig. 11

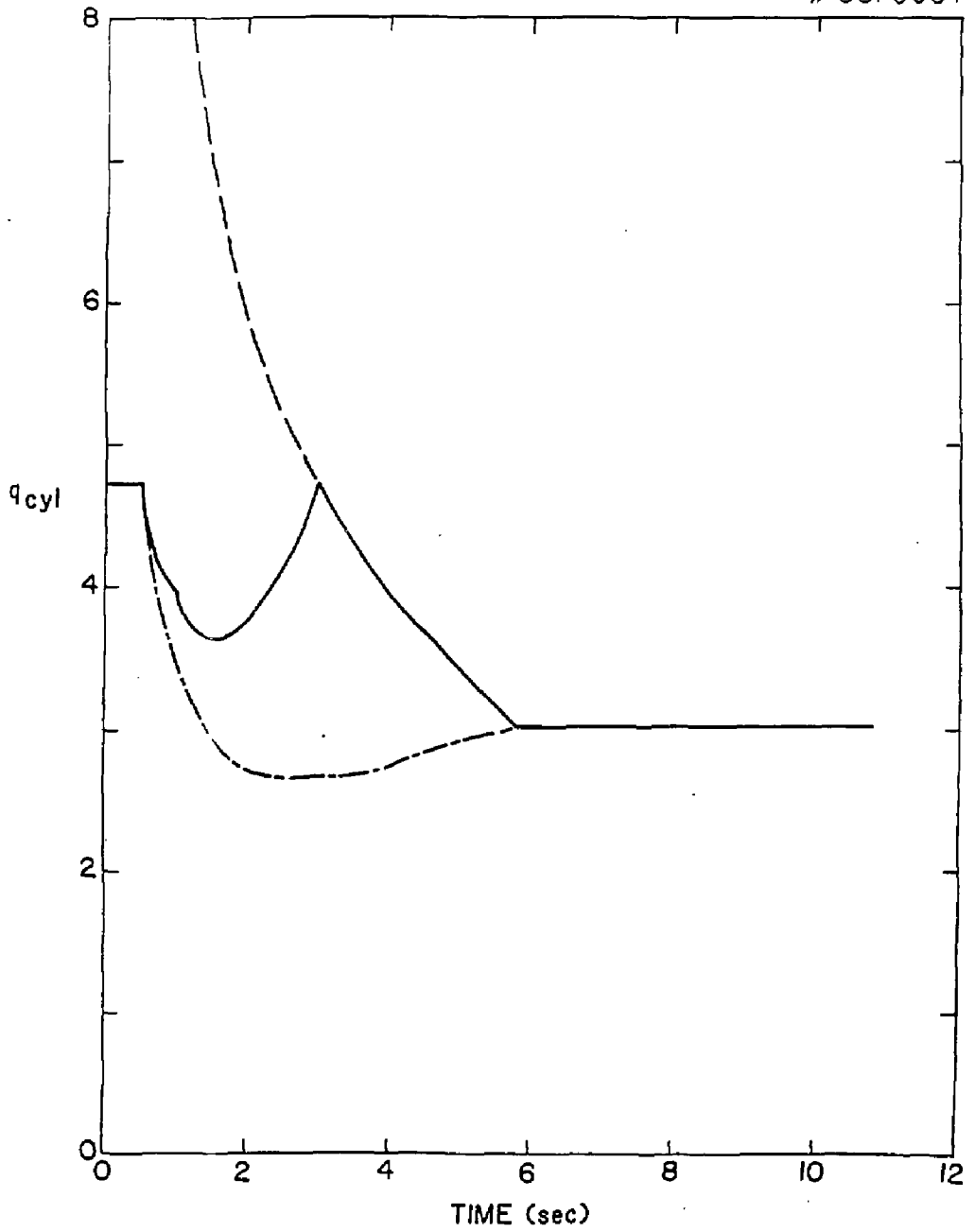


Fig. 12

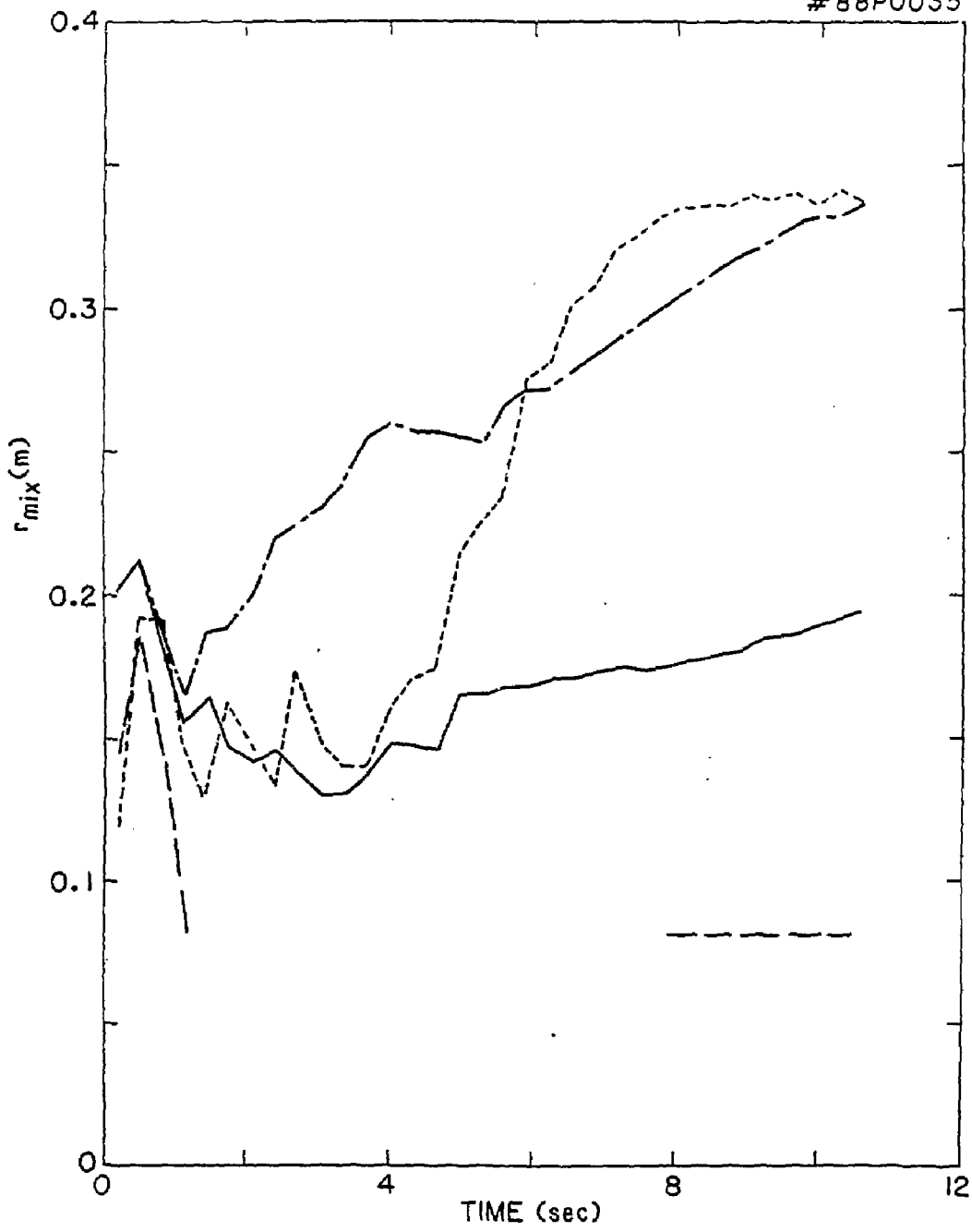


Fig. 13

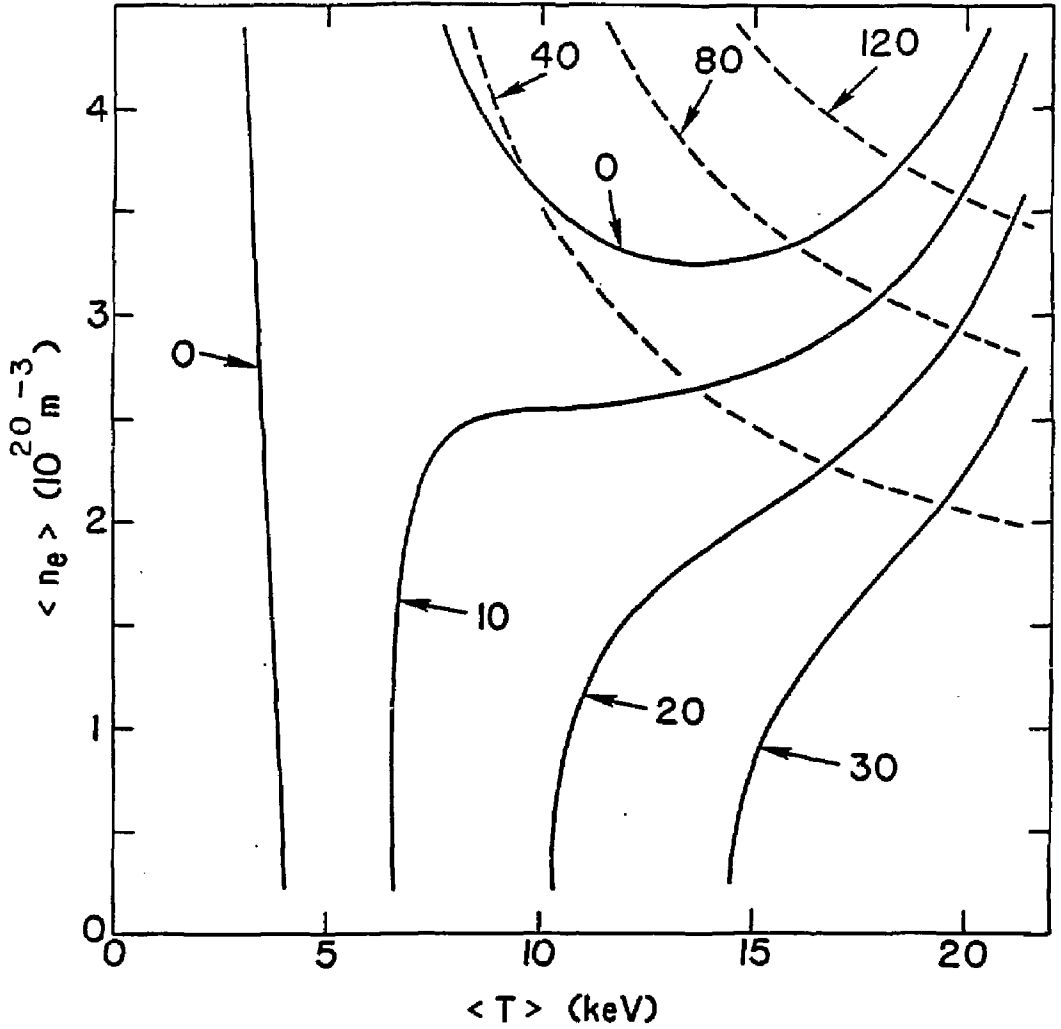
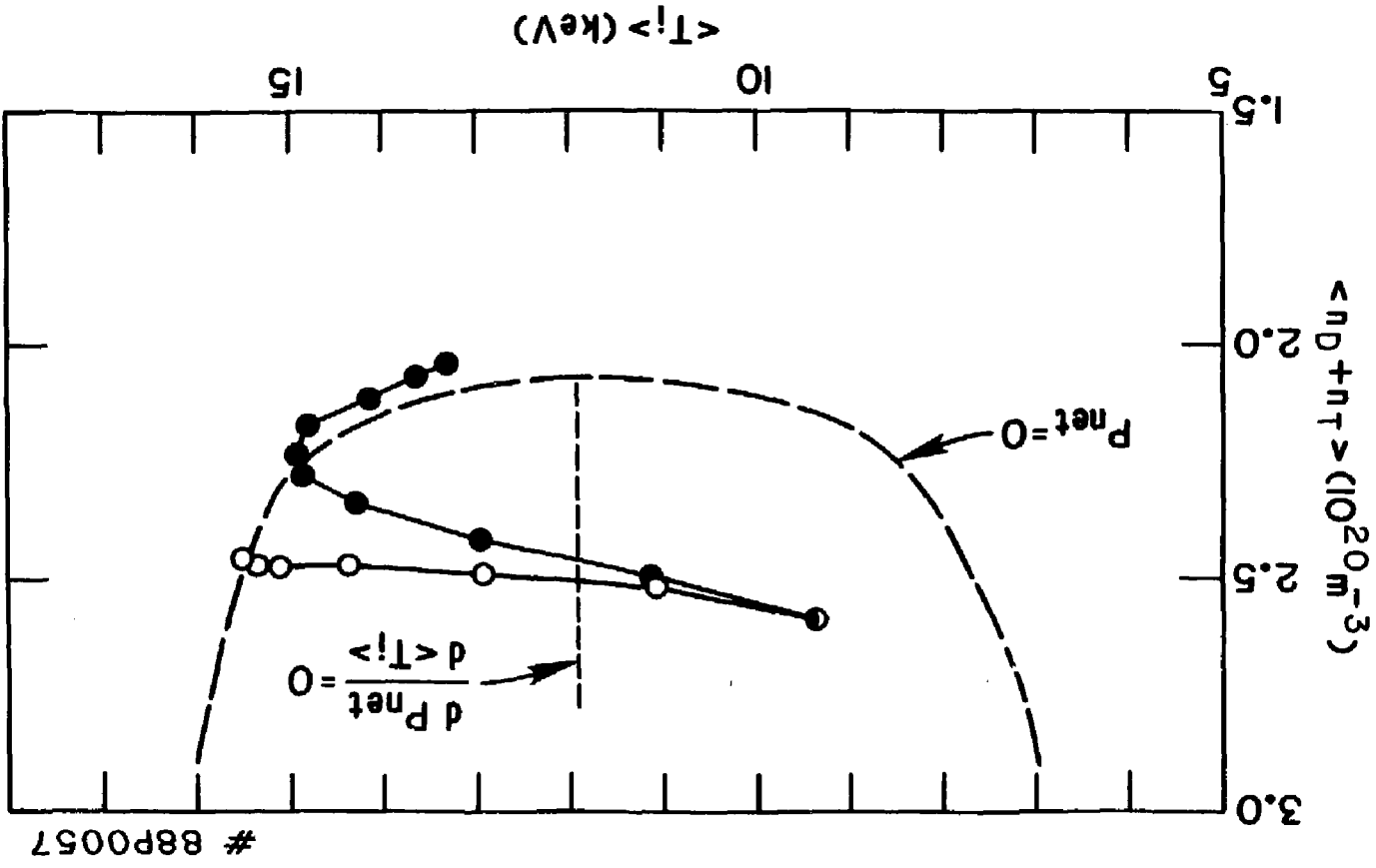


Fig. 14



88P0057

Fig. 15

EXTERNAL DISTRIBUTION IN ADDITION TO UC-20

Dr. Frank J. Paoloni, Univ of Wollongong, AUSTRALIA
Prof. M.H. Brennan, Univ Sydney, AUSTRALIA
Plasma Research Lab., Australian Nat. Univ., AUSTRALIA
Prof. I.R. Jones, Flinders Univ., AUSTRALIA
Prof. F. Cap, Inst Theo Phys, AUSTRIA
Prof. M. Heindler, Institut für Theoretische Physik, AUSTRIA
M. Goossens, Astronomisch Instituut, BELGIUM
Ecole Royale Militaire, Lab de Phys Plasmas, BELGIUM
Commission-Europeen, Dg-XII Fusion Prog, BELGIUM
Prof. R. Boucique, Laboratorium voor Natuurkunde, BELGIUM
Dr. P.H. Sakanaka, Instituto Fisica, BRAZIL
Instituto De Pesquisas Espaciais-INPE, BRAZIL
Documents Office, Atomic Energy of Canada Limited, CANADA
Dr. M.P. Bachynski, MPB Technologies, Inc., CANADA
Dr. H.M. Skarsgard, University of Saskatchewan, CANADA
Dr. H. Bernard, University of British Columbia, CANADA
Prof. J. Teichmann, Univ. of Montreal, CANADA
Prof. S.R. Sreenivasan, University of Calgary, CANADA
Prof. Tudor W. Johnston, INRS-Energie, CANADA
Dr. C.R. James, Univ. of Alberta, CANADA
Dr. Peter Lukac, Komenského Univ, CZECHOSLOVAKIA
The Librarian, Culham Laboratory, ENGLAND
The Librarian, Rutherford Appleton Laboratory, ENGLAND
Mrs. S.A. Hutchinson, JET Library, ENGLAND
C. Mouttet, Lab. de Physique des Milieux Ionisés, FRANCE
J. Radet, CEN/CADARACHE - Bat 506, FRANCE
Univ. of Ioannina, Library of Physics Dept. GREECE
Dr. Tom Muat, Academy Bibliographic Ser., HONG KONG
Preprint Library, Hungarian Academy of Sciences, HUNGARY
Dr. B. Dasgupta, Saha Inst of Nucl. Phys., INDIA
Dr. P. Kaw, Institute for Plasma Research, INDIA
Dr. Philip Rosenau, Israel Inst. Tech, ISRAEL
Librarian, Int'l Ctr Theo Phys, ITALY
Prof. G. Rostagni, Univ Di Padova, ITALY
Miss Clelia De Palo, Assoc EURATOM-ENEA, ITALY
Biblioteca, Instituto di Fisica del Plasma, ITALY
Dr. H. Yamato, Toshiba Res & Dev, JAPAN
Prof. I. Kawakami, Atomic Energy Res. Institute, JAPAN
Prof. Kyoji Nishikawa, Univ of Hiroshima, JAPAN
Dirac. Dept. Large Tokamak Res. JAERI, JAPAN
Prof. Satoshi Itoh, Kyushu University, JAPAN
Research Info Center, Nagoya University, JAPAN
Prof. S. Tanaka, Kyoto University, JAPAN
Library, Kyoto University, JAPAN
Prof. Nobuyuki Inoue, University of Tokyo, JAPAN
S. Mori, JAERI, JAPAN
Librarian, Korea Advanced Energy Res. Institute, KOREA
Prof. D.I. Choi, Adv. Inst Sci & Tech, KOREA
Prof. B.S. Liley, University of Waikato, NEW ZEALAND
Institute of Plasma Physics, PEOPLE'S REPUBLIC OF CHINA
Librarian, Institute of Phys., PEOPLE'S REPUBLIC OF CHINA
Library, Tsing Hua University, PEOPLE'S REPUBLIC OF CHINA
Z. Li, Southwest Inst. Physics, PEOPLE'S REPUBLIC OF CHINA
Prof. J.A.C. Cabral, Inst Superior Tecnico, PORTUGAL
Dr. Octavian Petrus, AL I CUZA University, ROMANIA
Dr. Johan de Villiers, Fusion Studies, AEC, SO AFRICA
Prof. M.A. Hellberg, University of Natal, SO AFRICA
C.I.E.M.A.T., Fusion Div. Library, SPAIN
Dr. Lennart Stenflo, University of UMEA, SWEDEN
Library, Royal Inst Tech, SWEDEN
Prof. Hans Wilhelmson, Chalmers Univ Tech, SWEDEN
Centre Phys des Plasmas, Ecole Polytech Fed, SWITZERLAND
Bibliotheek, Fom-Inst Voor Plasma-Fysica, THE NETHERLANDS
Dr. D.D. Ryufov, Siberian Acad Sci, USSR
Dr. G.A. Eliseev, Kurchatov Institute, USSR
Dr. V.A. Glukhikh, Inst Electrophysical Apparatus, USSR
Dr. V.T. Tolok, Inst. Phys. Tech. USSR
Dr. L.M. Kovrizhnykh, Institute Gen. Physics, USSR
Nuclear Res. Establishment, Julich Ltd., W. GERMANY
Bibliothek, Inst. Fur Plasmaforschung, W. GERMANY
Dr. K. Schindler, Ruhr Universitat Bochum, W. GERMANY
ASDEX Reading Rm, IPP/Max-Planck-Institut für
Plasmaphysik, W. GERMANY
Librarian, Max-Planck Institut, W. GERMANY
Prof. R.K. Janev, Inst Phys, YUGOSLAVIA